Electronic Supplementary Information

Enhancement of photocurrent by incorporation of Preyssler type polyoxometalate protected nanoparticles in polyporphyrin films

Zhaohui Huo,[ab] Yiming Liang,[b] Yaokang Lv,[bc] Fréderic Melin,[d] Petra Hellwig,[d] Helen Ibrahim, [e] Michel Goldmann,[e] Corinne Boudon,[b] Vasilica Badets,[b] Antoine Bonnefont,[b] and Laurent Ruhlmann[b*]

[a.] *Department of Chemistry, Guangdong University of Education, Guangzhou, 510303, PR China.*
[b.] *Université de Strasbourg, Institut de Chimie, UMR CNRS 7177, Laboratoire d'Electrochimie et de Chimie Physique du Corps Solide, 4 rue Blaise Pascal, CS 90032, 67081 Strasbourg cedex, France. E-mail: lruhlmann@unistra.fr.*
[c.] *College of Chemical Engineering and Materials Science, Zhejiang University of Technology, Hangzhou, 310014, China.*
[d.] *Chimie de la Matière Complexe UMR 7140, Laboratoire de Bioélectrochimie et Spectroscopie, CNRS-Université de Strasbourg, 4 rue Blaise Pascal, 67070 Strasbourg, France.*
[e.] *Sorbonne Universités, Institut des NanoSciences de Paris, UMR CNRS 7588, Université Paris 6, 4 place Jussieu, boîte courrier 840, F - 75252, Paris, France*

Acknowledgements
We thank CNRS, the Université de Strasbourg (France), Université Paris-Descartes (Paris, France), Sorbonne université (Paris, France) for funding of this work. We also thanks the Oversea Study Program of Guangzhou Elite Project (GEP) for the Ph.D. grant of Zhaohui Huo. The authors acknowledge Corinne Ulhaq-Bouillet (IPCMS, Strasbourg) for STEM characterization.

CONTENT

1. Experimental

Reagents. Most common laboratory chemicals were reagent grade, purchased from commercial sources and without further purification. Water was obtained by passing through a Milli-RO4 unit and subsequently through a Millipore Q water purification. Zinc-β-octaethylporphyrin, acetonitrile and dichloroethane were purchased from Sigma-Aldrich. Tetrabutylammonium hexaflurophosphate was purchased from Fluka. Sodium iodide was purchased from VWR® Prolabo and iodine was purchased from Panreac Quimica Sau.

The $K_{14}[NaP_5W_{30}O_{110}]$ was prepared according the literature procedure.[1]

1 a) I. Creaser, M. C. Heckel, R. J. Neitz, M. T. Pope, *Inorg. Chem*. 1993, **32**, 1573. b) Y. Jeannin, J. Martin-Frère, *Inorg. Synth.,* 1990, **27**, 115.

Electrochemistry and photoelectrochemistry Voltammetric and electrochemical impedance measurements have been performed with a standard three-electrode system using a PARSTAT 2273 potentiostat. Glassy carbon or single-side coated indium-tin-oxide (ITO, SOLEMS, 25-35 Ω/cm^{-2}) electrodes, with a surface of about 1 cm^2 have been used as working electrode. A platinum wire has been used as an auxiliary electrode. The reference electrode was a saturated calomel electrode. It was electrically connected to the solution by a junction bridge filled with the electrolyte. Photoelectrochemical responses for films were obtained by on-off light illumination of a 300 W Xe arc lamp (with $\lambda > 385$ nm long pass filter).

Electrochemical quartz crystal measurement (EQCM) A QCA-922 (SEIKO EG&G instrument) system combined with Versa STAT 3 was used for simultaneous quartz crystal measurement and cyclic voltammetric measurements. The electrochemical cell was assembled in a glove box using an ITO AT-cut quartz crystal resonator (mirror finished, resonant frequency: 9.08 MHz ± 50 kHz, A = 0.2 cm^2, SEIKO EG&G., LTD) as working electrode, a platinum wire as counter electrode, and a Ag/AgCl wire as a quasi-reference electrode.

UV–visible spectroscopic measurements UV–vis absorption spectra have been recorded on an Agilent 8453 spectrophotometer.

X-ray Photoelectron Spectroscopy (XPS). XPS experiments were carried out on a RBD upgraded PHI-5000C ESCA system (Perkin-Elmer) with MgKR radiation (*h* =1253.6 eV) or Al KR radiation (*h* = 1486.6 eV).

Atomic force micrographs (AFM) measurement. AFM have been conducted directly on the ITO surfaces using a Dimension 3100 (Veeco) in the tapping mode under ambient conditions. Silicon cantilevers (Veeco probes) with a spring constant of 300 N/m and a resonance frequency in the range of 120–139 kHz have been used. The scanning rate was 1.0 Hz.

Raman spectroscopy. Raman spectra were recorded on a Renishaw Invia Raman Microscope with the 457 or 514-nm emission line of an Ar-laser.

Transmission electronic microscopy (TEM). TEM observations were performed with a JEOL 100 CXII TEM instrument operated at an accelerating voltage of 100 kV.

Scan electronic microscopy (SEM). SEM measurements were performed using Jeol JSM-6700F (Japan) electron microscope with the lattice resolution of 1 nm, at accelerating voltage of 10 kV.

X-ray diffraction (XRD). X-ray diffraction using a Rigaku SmartLab diffractometer equipped with a rotating anode and monochromated CuK $\alpha 1$ radiation (λCu= 1.54056 Å).

Scanning transmission electron microscopy (STEM) - Energy Dispersive X-ray Spectroscopy (EDS). STEM-EDS elemental color mapping and Energy-Dispersive X-ray (EDX) analysis were performed using Jeol 2100F (200 kV).

2. Formation and characterization of P_5W_{30}@MNPs complexes

2.1 Photocatalytic synthesis of metal nanoparticles using Preyssler POM (P_5W_{30})

2.2 UV–Vis spectroscopy and TEM images of P_5W_{30}@MNPs

We present here a low ionic strength photolysis method with near-visible and UV light, which leads to the formation of metal nanoparticles, through a process in which POM serve both as reducing and stabilizer agent (Fig. S1). Specifically, three metal ions (Ag^+, $Au^{III}Cl_4^-$, and $Pt^{IV}Cl_6^{2-}$) can form metal nanoparticles in the presence of photochemically reduced POM in aqueous solutions. This reaction takes place at ambient temperature and without the addition of any stabilizer. A Preyssler-structure polyoxometalate, **$[NaP_5W_{30}O_{110}]^{14-}$** (**$P_5W_{30}$**) was chosen to form the **P_5W_{30}@MNPs**. Reduced **$[NaP_5W_{30}O_{110}]^{15-}$** ion was obtained by photolysis of a deaerated $[NaP_5W_{30}O_{110}]^{14-}$ aqueous solution with

λ > 240 nm light, in the presence of propan-2-ol as a sacrificial electron donor.

Fig. S2 shows the change of the UV-vis spectra during the photocatalysis for the formation of **P_5W_{30}@Ag**, **P_5W_{30}@Au** and **P_5W_{30}@Pt** nanoparticles respectively.

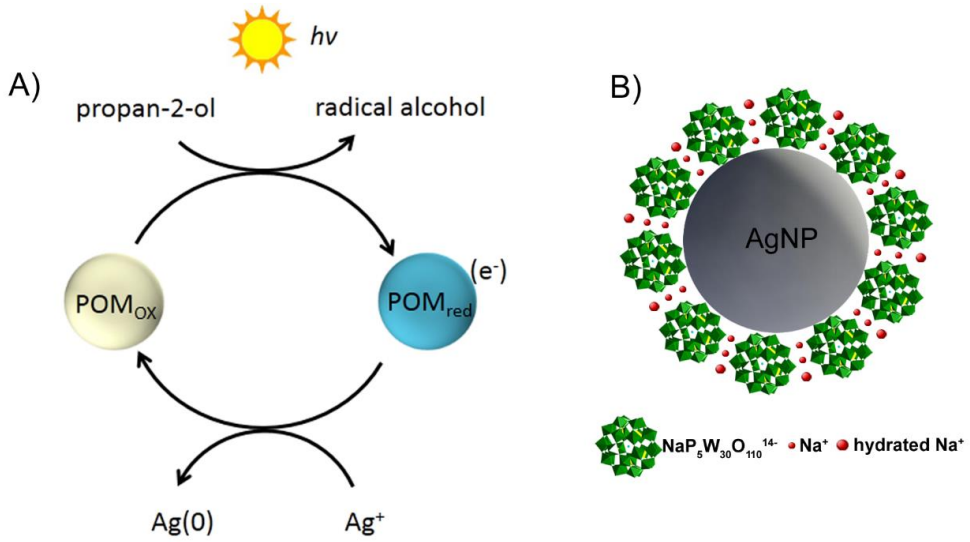

Fig. S1. A) Schematic mechanism of POM-catalyzed photochemical synthesis of Ag^+ to Ag(0) nanoparticles. B) Model structure of **P_5W_{30}@AgNPs**.

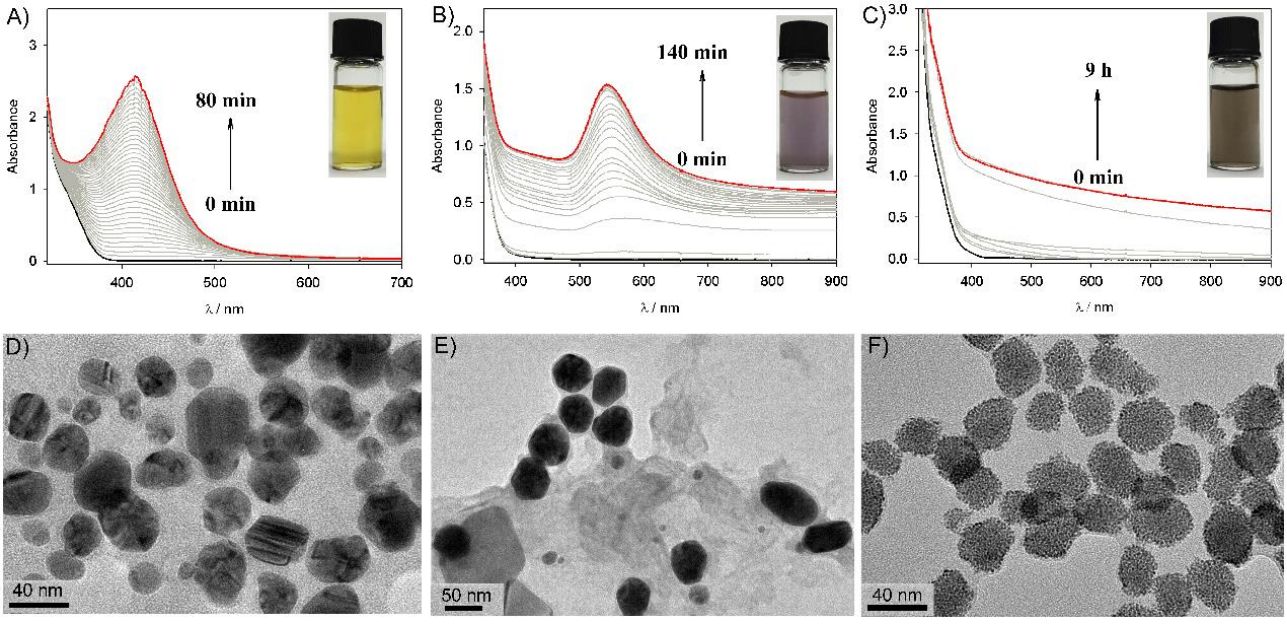

Fig. S2. Absorption spectra of metal nanoparticles (Ag, Au, Pt) in aqueous solution, obtained under UV-vis irradiation of **$K_{14}[NaP_5W_{30}O_{110}]$** (**$P_5W_{30}$**) with the corresponding metal ions A) $2Ag^+ SO_4^{2-}$ (0.2 mM), B) $K^+[AuCl_4]^-$ (0.4 mM) or C) $2H^+[PtCl_6]^{2-}$ (0.4 mM)) in the presence of 0.13 M propan-2-ol. Inset: photo of the getting metal nanoparticles in solutions. TEM images of D) **P_5W_{30}@Ag**, E) **P_5W_{30}@Au**, and F) **P_5W_{30}@Pt**.

2.3 X-ray diffraction (XRD)

The synthesized **P_5W_{30}@M** (M = Au, Ag, and Pt) nanoparticles have been deposited on ITO slide and then dried. All XRD measurements were recorded at ambient temperature.

The XRD patterns of the nanoparticles have been plotted in Figure S3. The crystallinity of synthesized **P_5W_{30}@M** (M = Au, Ag, and Pt) nanoparticles was confirmed and the corresponding XRD patterns are shown in Figure S3. For **P_5W_{30}@Au**, **P_5W_{30}@Au** and **P_5W_{30}@Pt**, the presence of the Preyssler type of polyoxometalate P_5W_{30} was observed with characteristic peaks at 2θ = 8.4, 10.9, and 16.9 (see also[1]). In the case of **P_5W_{30}@Au** nanoparticles additional diffraction peaks were detected at 2θ = 38.2 and 44.5 which correspond to the indexed planes (111) and (200) of the Au respectively.[2] Similarly, the XRD pattern of the **P_5W_{30}@Ag** nanoparticles shows the characteristic crystalline Ag face-centered cubic (fcc) phase withpeaks at 38.2 and 44.3 corresponding to the standard Bragg reflexion (111) and (200) respectively.[3] Finally, in the case of **P_5W_{30}@Pt** nanoparticles, XRD results confirmed the formation of crystalline Pt face-centered cubic (fcc) phase. The diffraction peaks at 2θ =39.9 and 46.2 correspond to the indexed planes (111), and (200)respectively which were consistent with the fcc structure of platinum.[4"]

1 A. Al-Shehri, and N. Katabathini, *Cat. Comm.*, 2018, **108**, 17-22.
2 D. V. Leff, L. Brandt, and J. R. Heath, *Langmuir*, 1996, **12**, 4723-4730.
3 P. Prakash, P. Gnanaprakasam, R. Emmanuel, S. Arokiyaraj, and M. Saravanan, *Colloids and Surfaces B: Biointerfaces*, 2013, **108**, 255e259.
4 R. Venu, T.S. Ramulu, S. Anandakumar, V.S. Rani and C.G. Kim, *Colloids Surf. A*, 2011, **384**, 733-738.

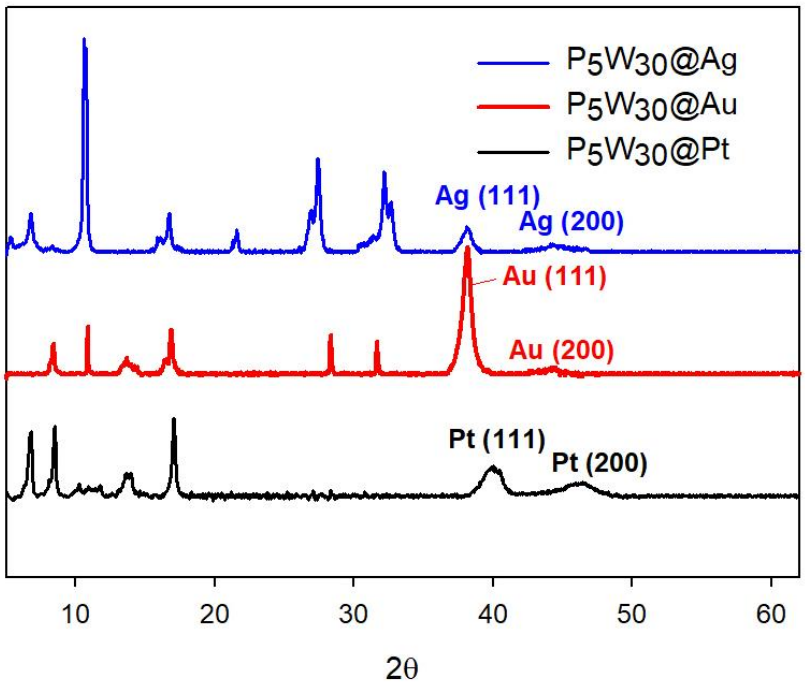

Fig. S3. XRD patterns of as-prepared a) **P_5W_{30}@Au**, b) **P_5W_{30}@Au** and c) **P_5W_{30}@Pt** nanoparticles.

2.4 Raman spectra of P_5W_{30}@MNPs

The raman spectrum of **$K_{14}[NaP_5W_{30}O_{110}]$** exhibits a major band at 968 cm^{-1} and a shoulder at 939 cm^{-1} (excitation wavelength of 457 and 514 nm), which can be attributed to the W=O and W-O-W stretches. Interestingly, in the spectra obtained at 514 nm, shoulders at 991 and 1003 cm^{-1} can also be observed. The P-O stretches probably contributes to the signal at 1003 cm^{-1}. Below 300 cm^{-1}, the W-O bending vibrations can be expected. Interaction with Au and Pt NPs does not induce major changes in the spectra. Interaction with AgNPs, however, dramatically enhances the intensity of the bands, and causes a 6 cm^{-1} downshift of the main band. A shoulder at 989 cm^{-1} is visible in both spectra taken at 457 and 514 nm. Silver nanoparticles exhibit several contributions in the 1300-1500 cm^{-1} spectral range.

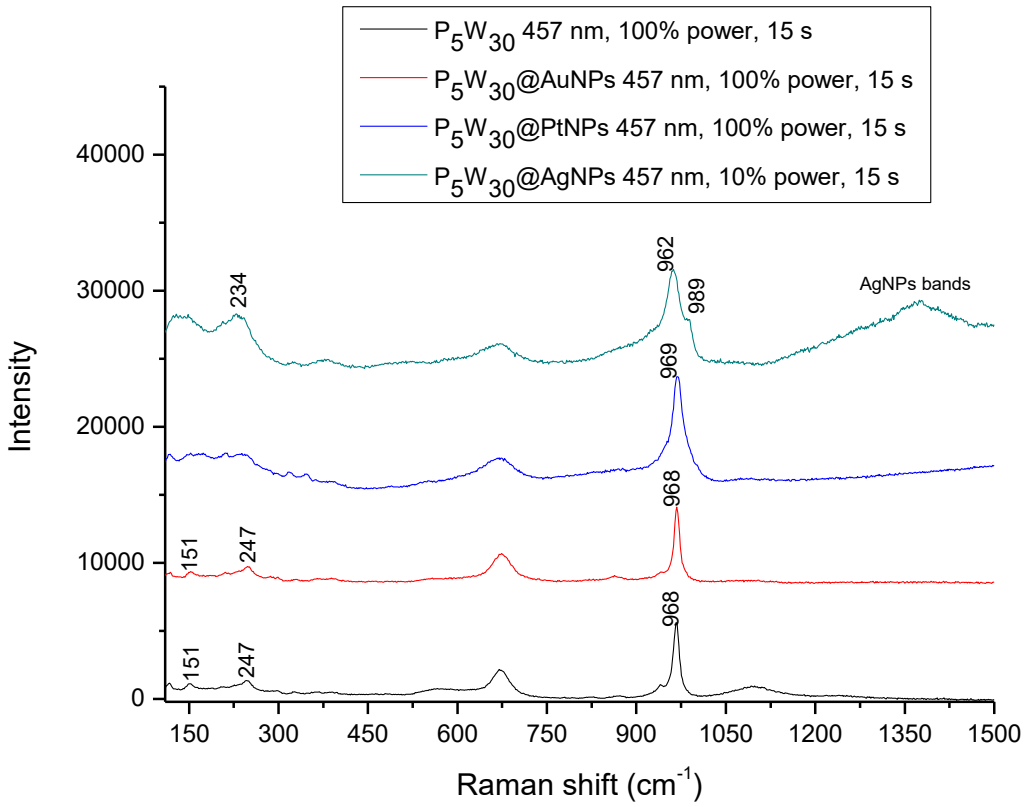

Fig. S4. Raman spectra of **P_5W_{30}@MNPs** excited at 457 nm.

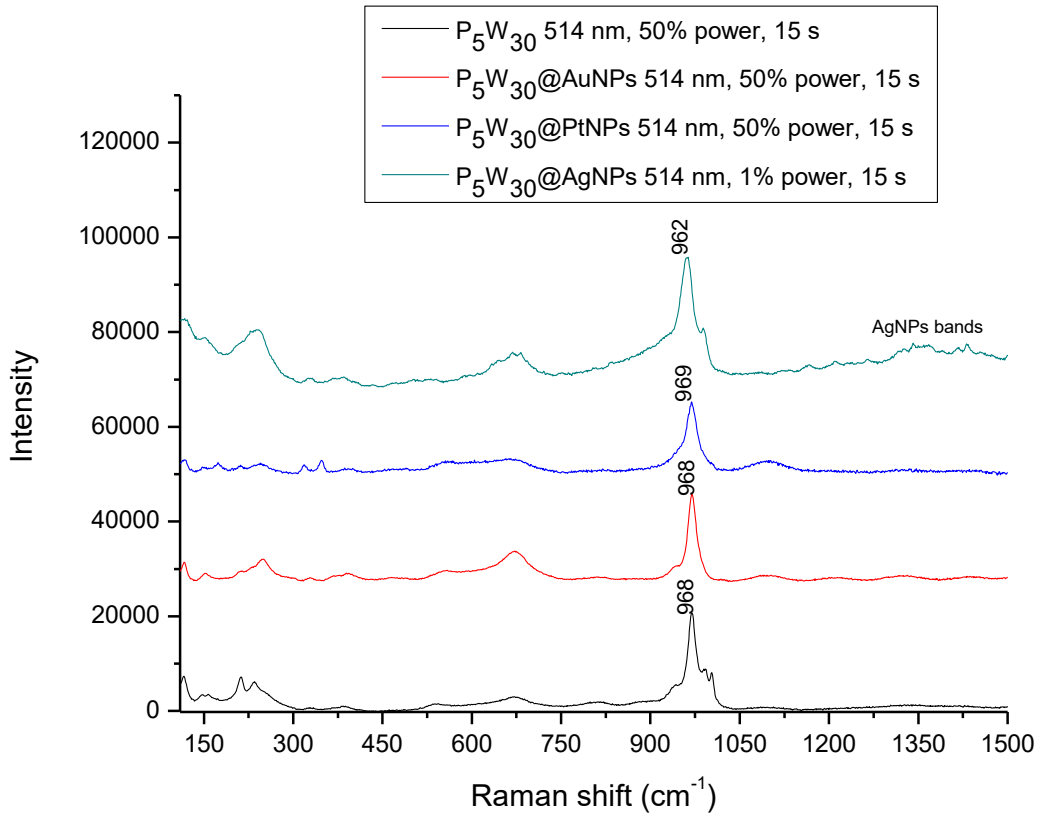

Fig. S5. Raman spectra of **P_5W_{30}@MNPs** excited at 514 nm.

3. Electropolymerization of Poly-*cis*-$H_2Ph_2Py_2P$-ZnOEP films and characterization

3.1 Electropolymerization of Poly-*cis*-$H_2Ph_2Py_2P$-ZnOEP films

Bis-porphyrin copolymers (Fig. S6) have been obtained by an electropolymerization process using **ZnOEP** macrocycle and one porphyrin functionalized by two pyridyl groups at the *meso* positions 5 and 10 (***cis*-$H_2Ph_2Py_2P$**). This electropolymerization process is based on a nucleophilic attack of the pyridyl groups onto electrogenerated **ZnOEP** dications. Note that ***cis*-$H_2Ph_2Py_2P$** functionalized by two pendant pyridyl groups can coordinated Zn atoms of **ZnOEP**, but due to the equilibrium with the porphyrin monomers **cis-$H_2Ph_2Py_2P$** and **ZnOEP**, it not prevents the electropolymerization.

The cyclic voltammograms recorded during electropolymerization of ***cis*-$H_2Ph_2Py_2P$** in the presence of **ZnOEP** shows the growths of three new waves in the cathodic part (Fig. S7), at least during the first sweeps (indeed, sometimes, the waves can merge each other when the scan numbers increase). These three waves are always absent during the first scan, i.e. before the oxidation of the **ZnOEP** ring. The first peak (peak*), around 0.0 and -0.2 V *vs.* SCE, corresponds to the reduction of the isoporphyrin which is formed during the electropolymerization process. The two other waves between -0.2 and -0.8 V *vs.* SCE are assigned to the reduction of the pyridinium spacers which are formed between each macrocycle within the polymeric chain.

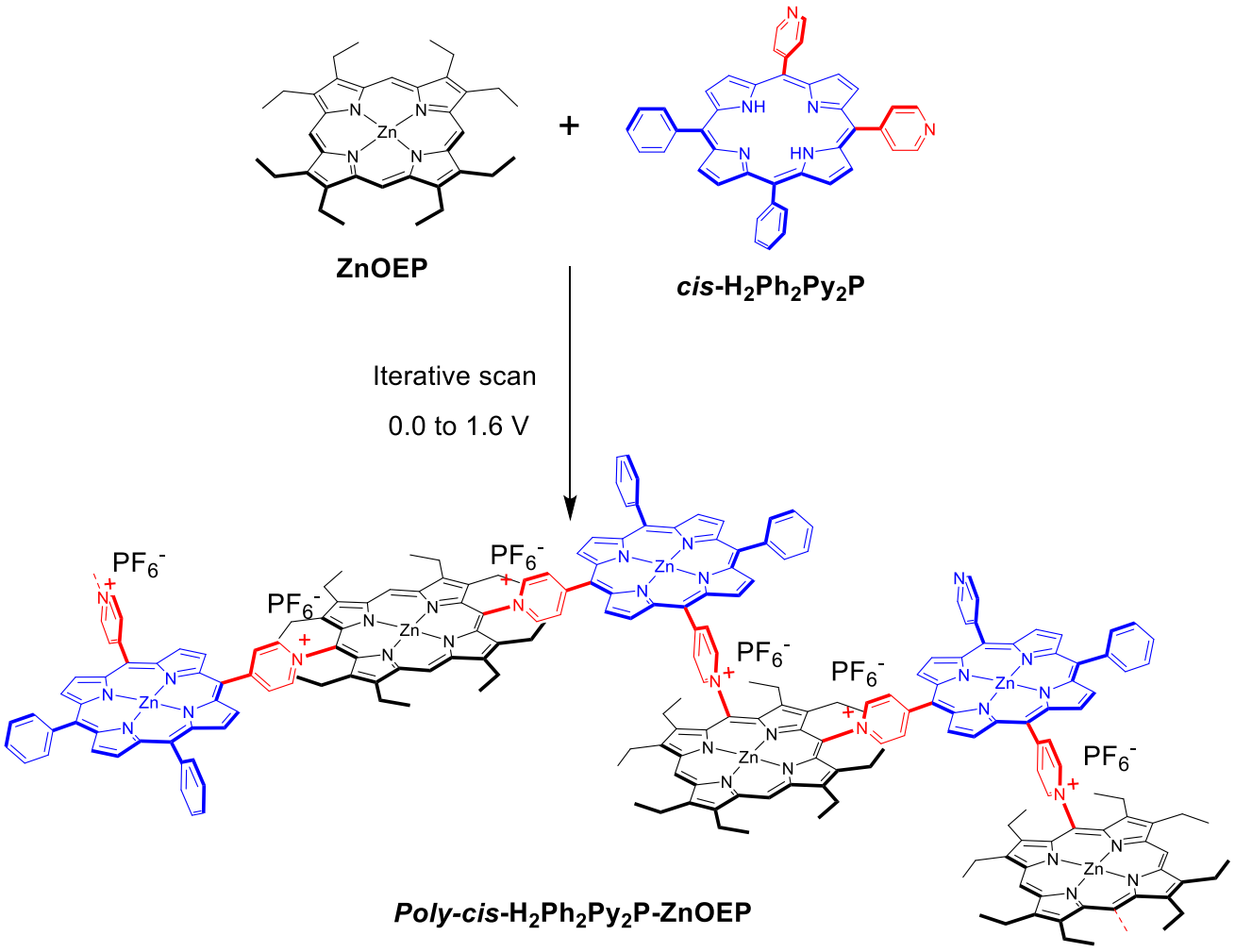

Fig. S6. Electropolymerization scheme of **ZnOEP** in the presence of ***cis*-$H_2Py_2Ph_2P$**.

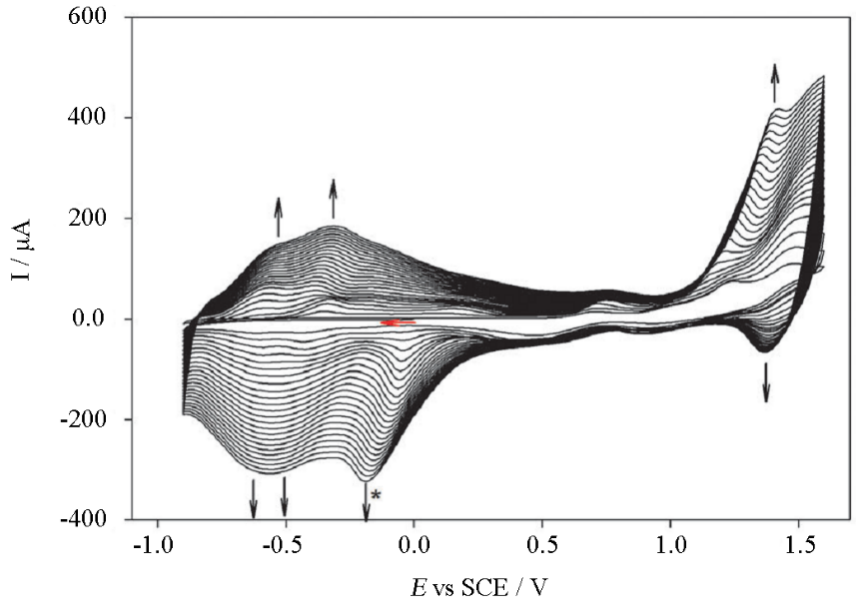

Fig. S7. Cyclic voltammograms recorded during 25 iterative scans in a 1,2-$C_2H_4Cl_2$/CH_3CN (7/3) solution of **ZnOEP** (0.25 mmol L^{-1}) in the presence of ***cis*-$H_2Py_2Ph_2P$** (0.25 mmol L^{-1}) and $TBAPF_6$ (0.1 mol L^{-1}). WE: ITO. S = 1 cm^2. *v* = 0.2 V s^{-1}. (*) This wave is attributed to the reduction of an isoporphyrin intermediate.

An $E(EC_N\ meso EC_B)_nE$ mechanism is proposed to account for the electropolymerization process where EE relates to the first and second oxidation of the porphyrin and C_N *meso* corresponds to the nucleophilic attack at the meso position of the porphyrin to yield an isoporphyrin intermediate.8 This latter compound is then oxidized (electrochemical step) and the hydrogen atom initially located on the meso-carbon is released (chemical step C_B). The electropolymerization can be conducted by iterative scan between 0.00 and +1.60 V in the presence of **ZnOEP** and ***cis*-$H_2Py_2Ph_2P$** as shown in Figure S6.

The electrosynthesis process of **Poly-*cis*-$H_2Ph_2Py_2P$-ZnOEP** between 0.00 and +1.60 V has been monitored by EQCM. Fig. S8 shows the simultaneously recorded cyclic voltammograms and mass changes. The change in the quartz resonance frequency (Δf) allows the calculation of the deposited mass (Δm) using the Sauerbrey's equation. A significat decrease of frequency is observed during the second oxidation peak, meaning that the electropolymerization happens during the formation of the porphyrin dication. After each electropolymerisation cycle, the frequency is decreased and the deposited mass is increased (Fig. S8B).

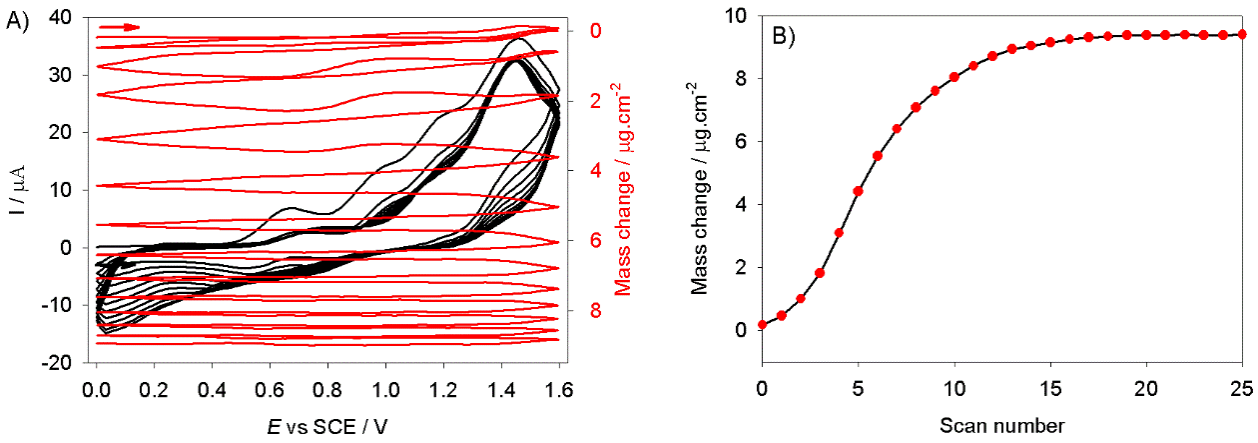

Fig. S8. A) Consecutive cyclic voltammograms (first 15 scans) and electrochemical quartz crystal microbalance measurements for the first 15 scans during the electropolymerization of 0.25 mmol L^{-1} **ZnOEP** with 0.25 mmol L^{-1} ***cis*-$H_2Py_2Ph_2P$** in CH_3CN/1,2-$C_2H_4Cl_2$ (3/7) in the presence of 0.1 mol L^{-1} $TBAPF_6$. Working electrode: ITO (A = 0.2 cm^2) deposited on a 9.08 MHz AT-cut quartz crystal. *v* = 100 mV s^{-1}. B) Mass change (Δm) calculated from Sauerbrey's equation versus the number of scan n.

The steady change of the frequency with time was an indication of the smooth increase of the copolymer mass. The mass increases with a quasi linear variation during the first ten scans. The electrode coverage with the deposited film after 25 iterative scans was 9.4 µg cm^{-2}.

3.2 Film Morphology (Atomic Force Microscopy)

The coated electrodes were washed with CH_2Cl_2 to remove any residual of the conducting salt present on the film. In a typical AFM image, **Poly-*cis*-$H_2Py_2Ph_2P$-ZnOEP** appeared as tightly packed coils with average diameters of 100 ± 10 nm and a height of 13.0 ± 1.0 nm a (Fig. S9). The root mean square (RMS) surface roughness of the film obtained from 0 to +1.60 V vs. SCE were 2.20 nm after n=3 iterative scans and 5.33 nm after n=25 iterative scans in an area of 25 μm^2.

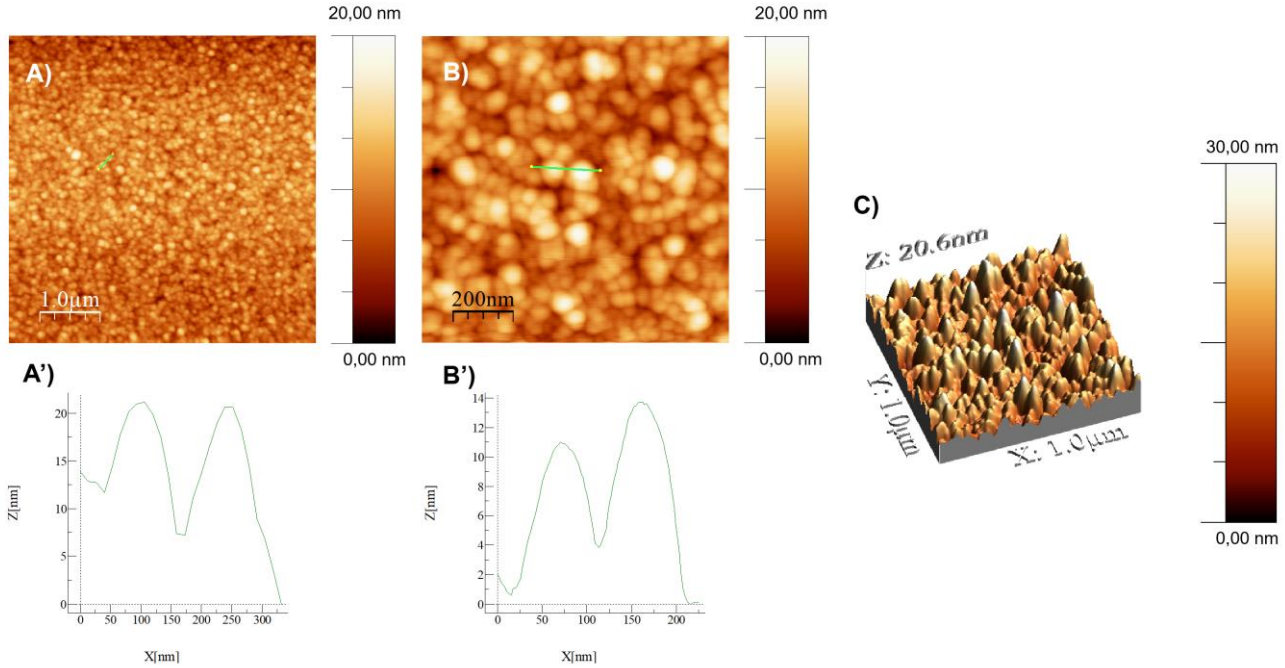

Fig. S9. Tapping mode AFM topography of A) and B) **Poly-*cis*-$H_2Ph_2Py_2P$-ZnOEP**, and A') and B') section analysis of the aggregate marked by a green line. C) 3D View.

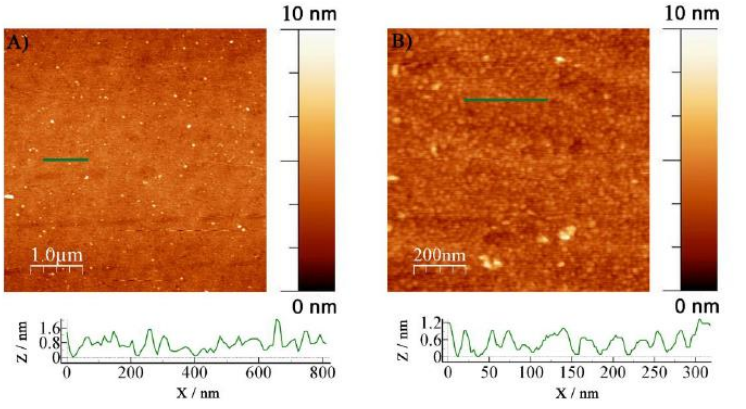

Fig. S10. Tapping mode AFM topography of A) and B) nude ITO and section analysis marked by blue lines for A) and B).

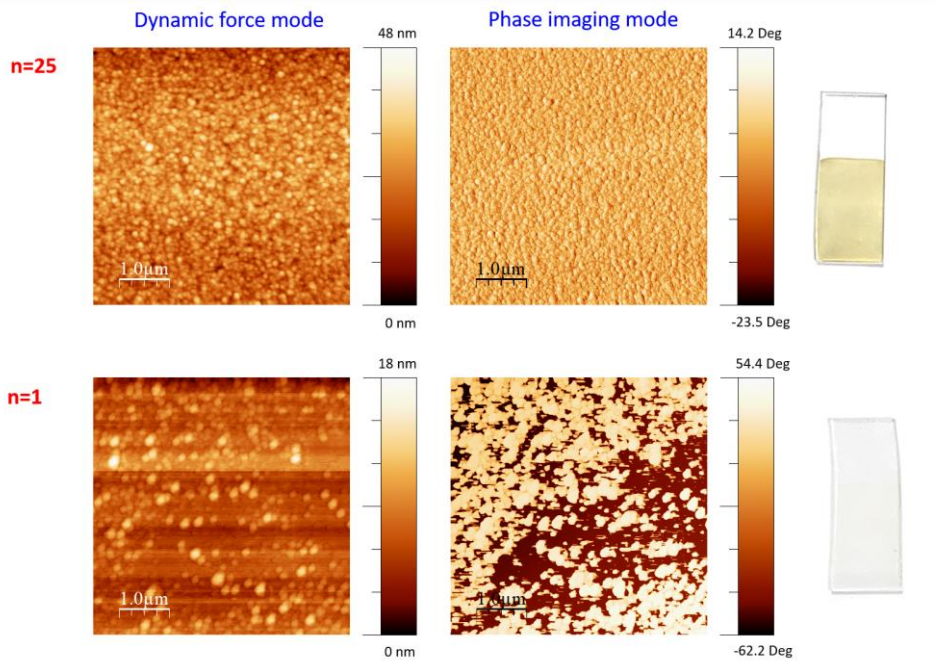

Fig. S11. AFM topography of **Poly-*cis*-$H_2Ph_2Py_2P$-ZnOEP** obtained after 25 and 1 iterative scan(s) between 0 and 1.6 V. Left pictures: dynamic force mode (tapping mode, Height). Middle pictures: phase imaging mode. Rigth pictures: photos of the ITO slides.

In ***Dynamic force mode*** also known as tapping mode: a stiff cantilever is oscillating closer to the sample than in noncontact mode. Part of the oscillation extends into the repulsive regime, so the tip intermittently "touches or taps" the surface.

In ***Phase imaging mode***, the phase shift of the oscillating cantilever relative to the driving signal is measured. This phase shift can be correlated with specific material surface properties that effect the tip/sample interaction. The phase shift can be used to differentiate areas on a sample with such differing properties as friction, adhesion and viscoelasticity.

The phase signal was described as being sensitive to variations in composition, adhesion, friction, viscoelasticity.

The technique is used simultaneously with dynamic force mode so topography can be measured as well. On Figure S11, one clearly observes that, for n = 25, the phase shift remains uniform on the surface with a variation lower than 5° (upper middle image) as for n =1 (lower middle image) this variation reaches more than 100° indicating anong uniform film. From the measurements, we consider that the surface is fully and homogeneously covered for n = 25, contrary to the case n= 1.

4. Fabrication and characterization of Poly-*cis*-$H_2Ph_2Py_2P$-ZnOEP/Preyssler POM@MNPs films

4.1 POM@MNPs ligand exchange with PF_6^- monitored via QCM

In order to monitor the exchange between the PF_6^- counterion of the **Poly-*cis*-$H_2Py_2Ph_2P$-ZnOEP** film

and the POM@MNPs, the polymer film was pre-deposited on the ITO quartz resonator. The change in the resonator frequency upon the contact of the POM@MNPs solution with the film is depicted in Figures S12, S13 and S14. In order to measure only the Δf due to the immobilization of POM@MNPs via ligand exchange and electronic interactions and to exclude the unspecific adsorption, a washing step with H_2O was also monitored. It can be observed that the washing step eliminates the weakly adsorbed POM@MNPs. Multiple cylcles of immobilization and washing were performed in order to measure the immobilization kinetics (Fig. S12B, S13B and S14B).

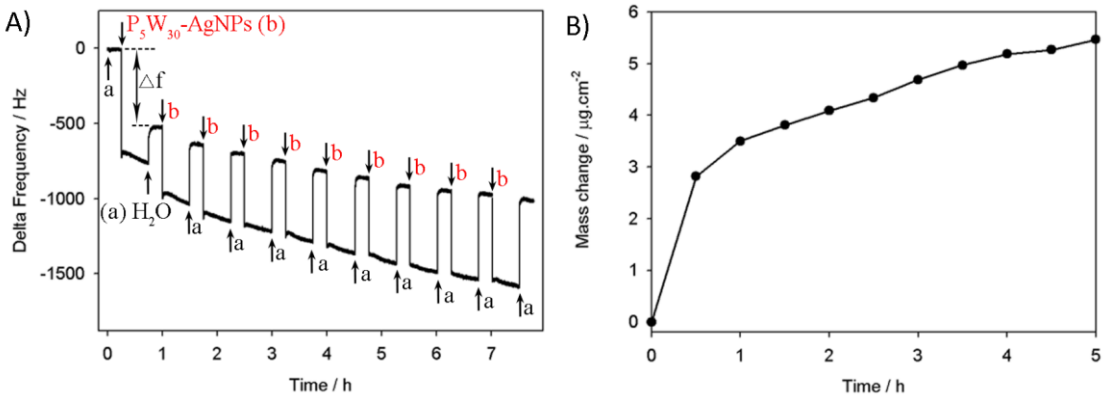

Fig. S12. Frequency response of QCM sensor to **P_5W_{30}@Ag** (**$[NaP_5W_{30}O_{110}]^{14-}$@AgNPs**) (named b) adsorption onto the **Poly-*cis*-$H_2Py_2Ph_2P$-ZnOEP** film (pre-electrodeposited onto a 9.08 MHz AT-cut quartz resonator with a thin ITO layer (A = 0.2 cm^2)). The start base line was obtained when the sensor was exposed to H_2O (named a). The arrows ↓ indicated the injection of **P_5W_{30}@Ag**. The arrow ↑ indicated the washing using H_2O. B) Mass change (Δm) calculated from Sauerbrey's equation versus the soaking time.

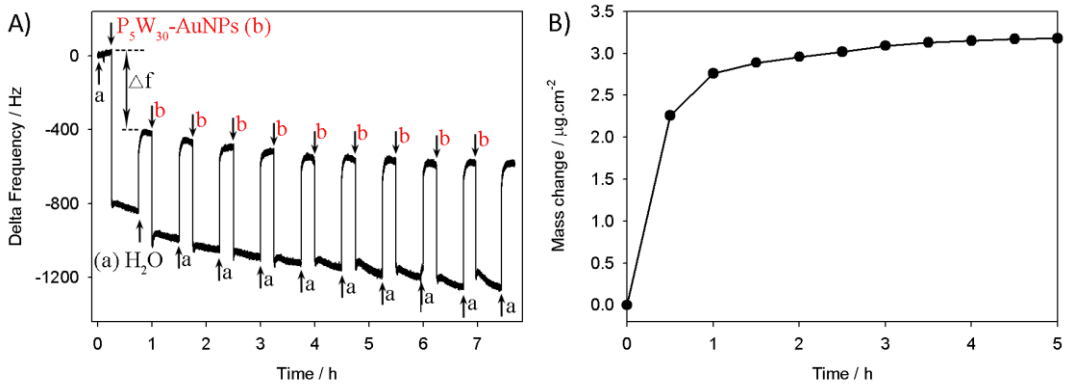

Fig. S13. Frequency response of QCM sensor to **P_5W_{30}@Au** (**$[NaP_5W_{30}O_{110}]^{14-}$@Au**) (named b) adsorption onto the **Poly-*cis*-$H_2Py_2Ph_2P$-ZnOEP** film (pre-electrodeposited onto a 9.08 MHz AT-cut quartz sonator with a thin ITO layer (A = 0.2 cm^2))**.** The start base line was obtained when the sensor was exposed to H_2O (named a). The arrows ↓ indicated the injection of $[NaP_5W_{30}O_{110}]^{14-}$@Pt. The arrow ↑ indicated the washing using H_2O. B) Mass change (Δm) calculated from Sauerbrey's equation versus the soaking time.

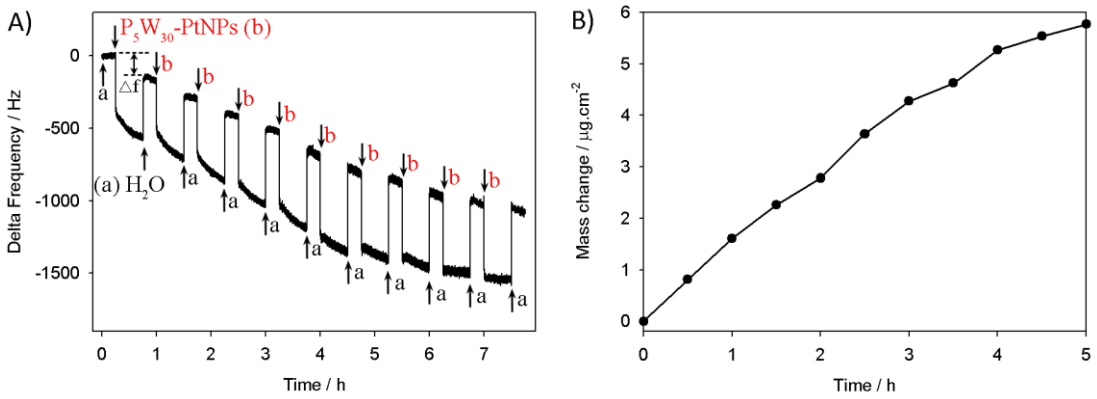

Fig. S14. Frequency response of QCM sensor to **P_5W_{30}@Pt** (**$[NaP_5W_{30}O_{110}]^{14-}$@Pt**) (named b) adsorption onto the **Poly-*cis*-$H_2Py_2Ph_2P$-ZnOEP** film (pre-electrodeposited onto a 9.08 MHz AT-cut quartz sonator with a thin ITO layer (A = 0.2 cm^2))**.** The start base line was obtained when the sensor was exposed to H_2O (named a). The arrows ↓ indicated the injection of $[NaP_5W_{30}O_{110}]^{14-}$@Pt. The arrow ↑ indicated the washing using H_2O. B) Mass change (Δm) calculated from Sauerbrey's equation versus the soaking time.

Table S1. Mass change (Δm) calculated from Sauerbrey's equation versus the soaking time.

Time (h)	Δm after adsorption of **P_5W_{30}@AgNPs** (µg.cm^{-2})	Δm after adsorption of **P_5W_{30}@AuNPs** (µg.cm^{-2})	Δm after adsorption of **P_5W_{30}@PtNPs** (µg.cm^{-2})
0.0	0.00	0.00	0.00
0.5	2.82	2.26	0.81
1.0	3.50	2.76	1.61
1.5	3.81	2.89	2.26
2.0	4.09	2.96	2.78
2.5	4.34	3.02	3.64
3.0	4.69	3.09	4.28
3.5	4.97	3.13	4.63
4.0	5.19	3.15	5.27
4.5	5.27	3.17	5.54
5.0	5.47	3.18	5.77

4.2 Evolution of UV-vis spectra during the attachement of POM@MNPs on the copolymer film

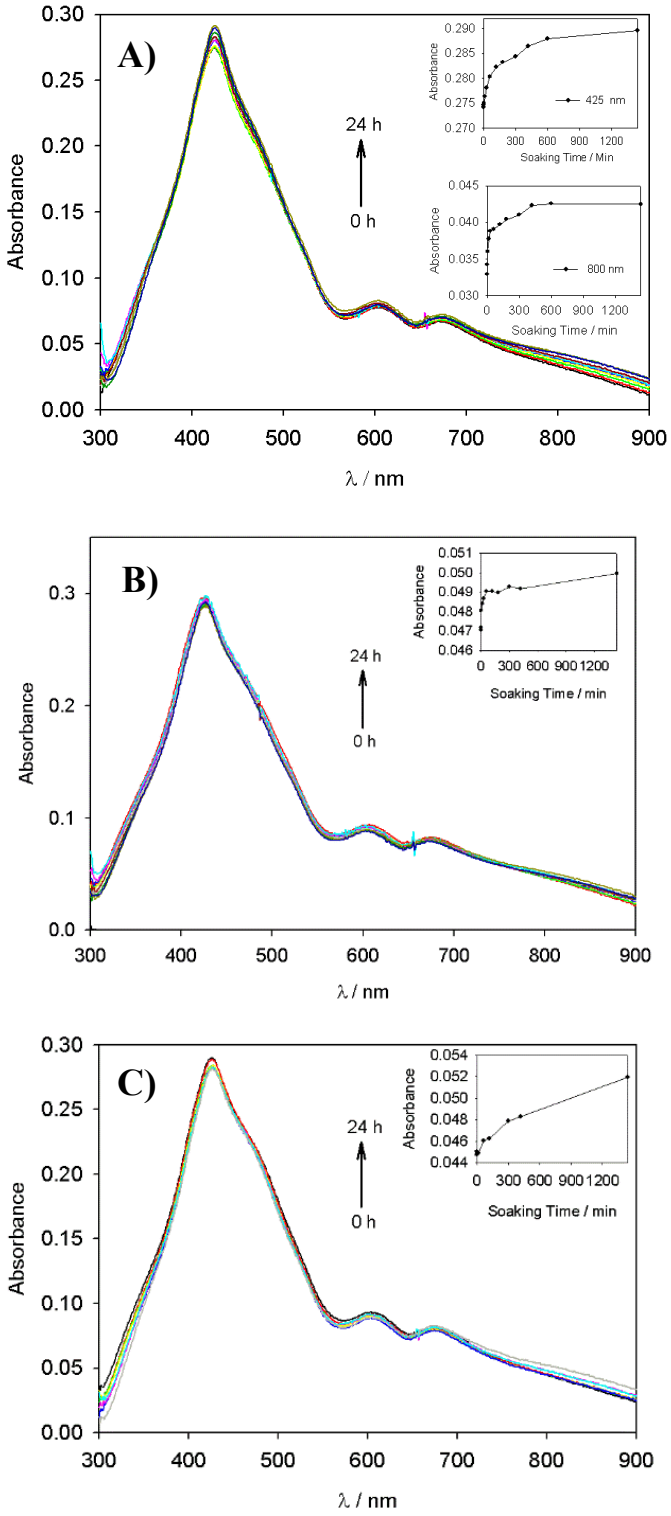

Fig. S15. Evolution of UV-vis spectra of the modified ITO electrode with **Poly-*cis*-$H_2Ph_2Py_2P$-ZnOEP** after soaking in A) **P_5W_{30}@Ag**, B) **P_5W_{30}@Au** and C) **P_5W_{30}@Pt** aqueous solution. Inset: absorbance intensity at λ = 425 nm, λ = 800 nm (A) and λ = 800 nm (B and C) *vs.* time.

The electrostatic interaction between the **Poly-*cis*-$H_2Ph_2Py_2P$-ZnOEP film** and the **P_5W_{30}@MNPs** was followed by UV-Vis absorption measurements. Figure S15 shows the evolution of the absorption spectra of the **Poly-*cis*-$H_2Ph_2Py_2P$-ZnOEP** film with different soaking time in the **P_5W_{30}@MNPs** solution where

M = Ag, Au or Pt. In the absence of **P_5W_{30}@MNPs** the spectra contain the expected Soret and Q bands of the immobilized porphyrins. In the presence of the **P_5W_{30}@Ag** the intensity at 425 nm slightly increases with time (see inset of Fig S15A), showing the immobilization of the nanoparticles on the film (the surface plasmon of Ag NPs is at λ_{max} = 433nm (Fig. S15A)). In the presence of **P_5W_{30}@MNPs** the intensity at 800 nm slightly increases with time. This is attributed to the agglomeration of the nanoparticles at the film surface. It must be noticed here that the strongest interaction is observed between the film and the the **P_5W_{30}@Ag.**

4.3 X-ray photoelectron spectra of Poly-*cis*-$H_2Ph_2Py_2P$-ZnOEP/P_5W_{30}@MPNs

XPS analysis of the obtained films confirms the success of the immobilization of P_5W_{30}@MNPs or P_5W_{30} even if some PF_6^- still remained in the film.

Figure S16 reveals XPS spectrum of **Poly-*cis*-$H_2Py_2Ph_2P$-ZnOEP** films. The XPS survey spectrum of the composite material in Figure S14 indicates the presence of C, O, N, Zn, P, and F elements, which is consistent with the composition of the copolymer.

In the case of **Poly-*cis*-$H_2Py_2Ph_2P$-ZnOEP/P_5W_{30}**, additional XPS peaks located at 37.9 eV and 35.8 eV, which are attributed to W 4f5/2, and to W 4f7/2 respectively (Fig. S17). These values are in agreement with the values for W(VI). At the same time important decrease of the F 1s peak at 687.2 eV and the modification of the P $2P_{3/2}$ signal from 138.3 eV (PF_6^-) to 133.8 eV ($[NaP_5W_{30}O_{110}]^{14-}$) indicate the exchange of PF_6^- by the Preyssler type polyoxometalate ($[NaP_5W_{30}O_{110}]^{14-}$) (Fig. S18).

Immobilization of P_5W_{30}@MNPs is also confirm by XPS analysis. Figure S19 gives the XPS peaks of **Poly-*cis*-$H_2Py_2Ph_2P$-ZnOEP-P_5W_{30}@Ag** film showing the Ag 3d signal. The high-resolution Ag 3d spectrum shows two peaks are located at 374.2 eV and 368.0 eV, which are corresponding to the values for zero valent Ag, standing for Ag 3d3/2 and Ag 3d5/2, respectively. The presence of tungsten was also determined by XPS. The W 4f 5/2 and 4f 7/2 doublet with the binding energies is found in 37.9 eV and 35.8 eV respectively. These values exhibit full oxidation form of tungsten (W(VI)) in $[NaP_5W_{30}O_{110}]^{14-}$. The above results strongly prove that metallic Ag and tungstophosphate are successfully exchanged PF_6^- to the **Poly-*cis*-$H_2Py_2Ph_2P$-ZnOEP** surface.

Similar result has been obtained for **Poly-*cis*-$H_2Py_2Ph_2P$-ZnOEP-P_5W_{30}@Au** (Fig. S20) showing the Au 4f 7/2 and 4f 5/2 doublet with the binding energies of 84.2 eV and 87.4 eV, respectively (Fig. S20). In the case of and **Poly-*cis*-$H_2Py_2Ph_2P$-ZnOEP-P_5W_{30}@Pt,** the Pt 4f 7/2 and 5/2 doublet located at 70.9 eV and 74.2 eV are observed and correspond to the values for zero valent Pt, standing for Pt 4f7/2 and Pt 4f5/2, respectively (Fig. S21).

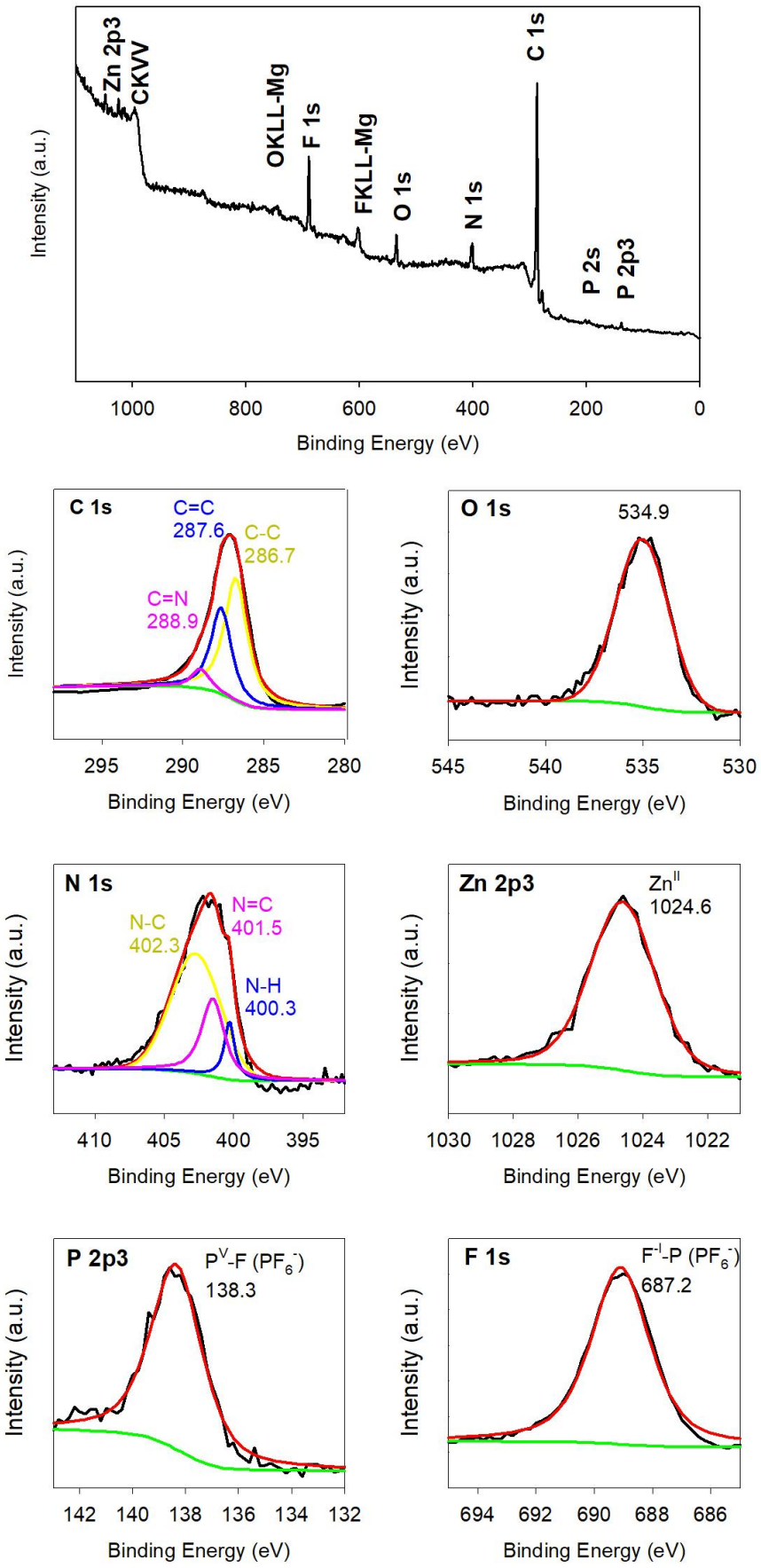

Fig. S16. XPS of **Poly-*cis*-$H_2Py_2Ph_2P$-ZnOEP** films on ITO.

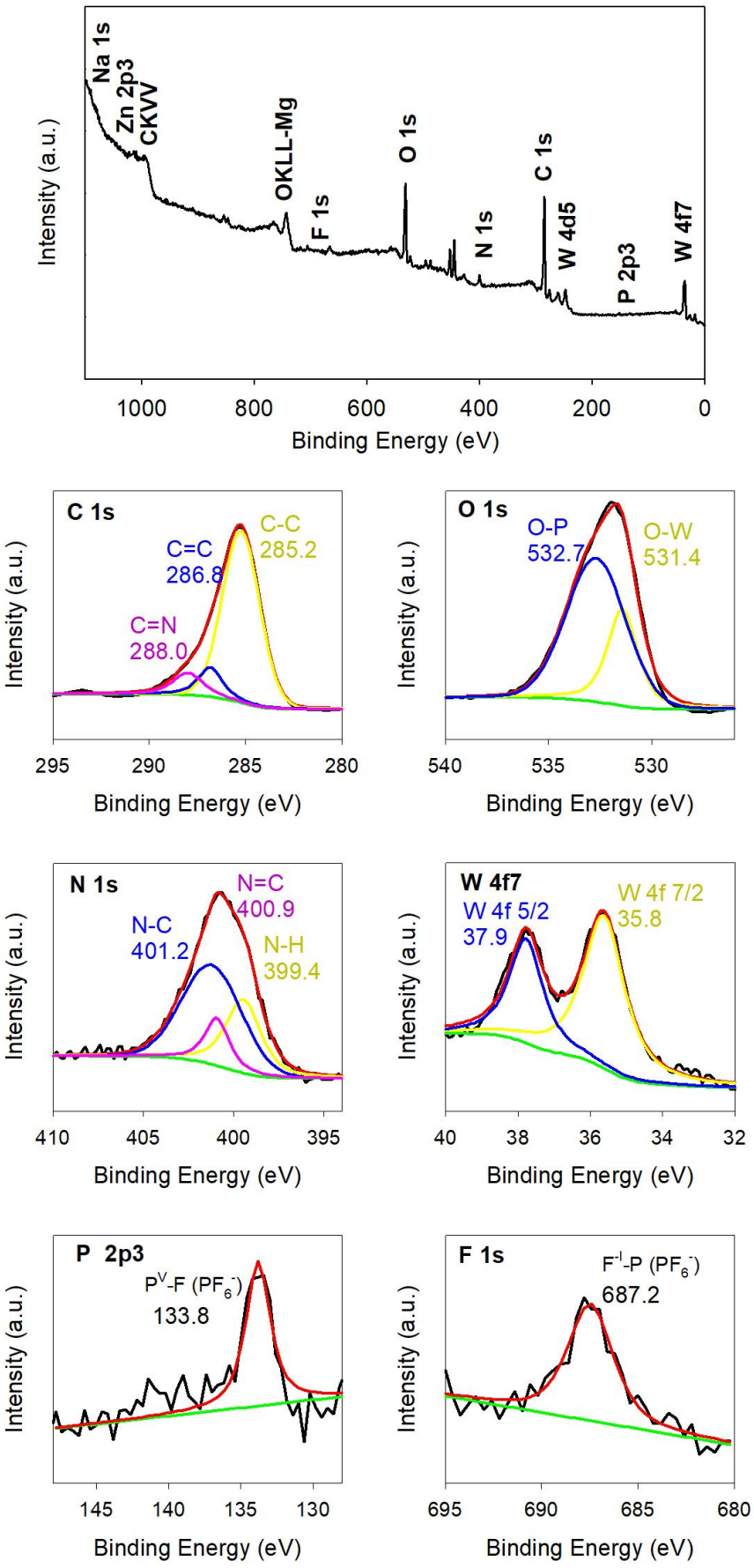

Fig. S17. XPS of **Poly-*cis*-$H_2Py_2Ph_2P$-ZnOEP/P_5W_{30}** films on ITO.

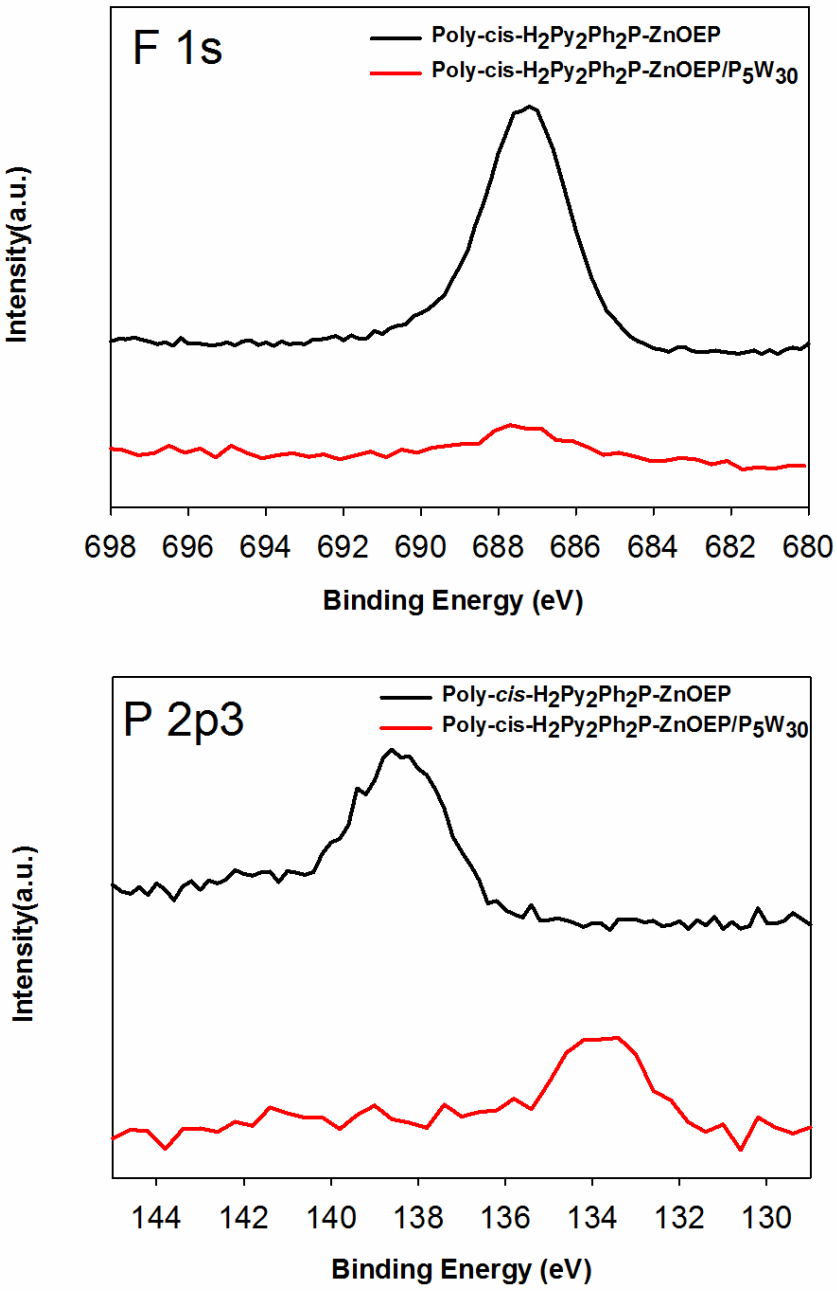

Fig. S18. Comparaison of XPS spectra of **Poly-*cis*-$H_2Py_2Ph_2P$-ZnOEP and of Poly-*cis*-$H_2Py_2Ph_2P$-ZnOEP/P_5W_{30}** films on ITO.

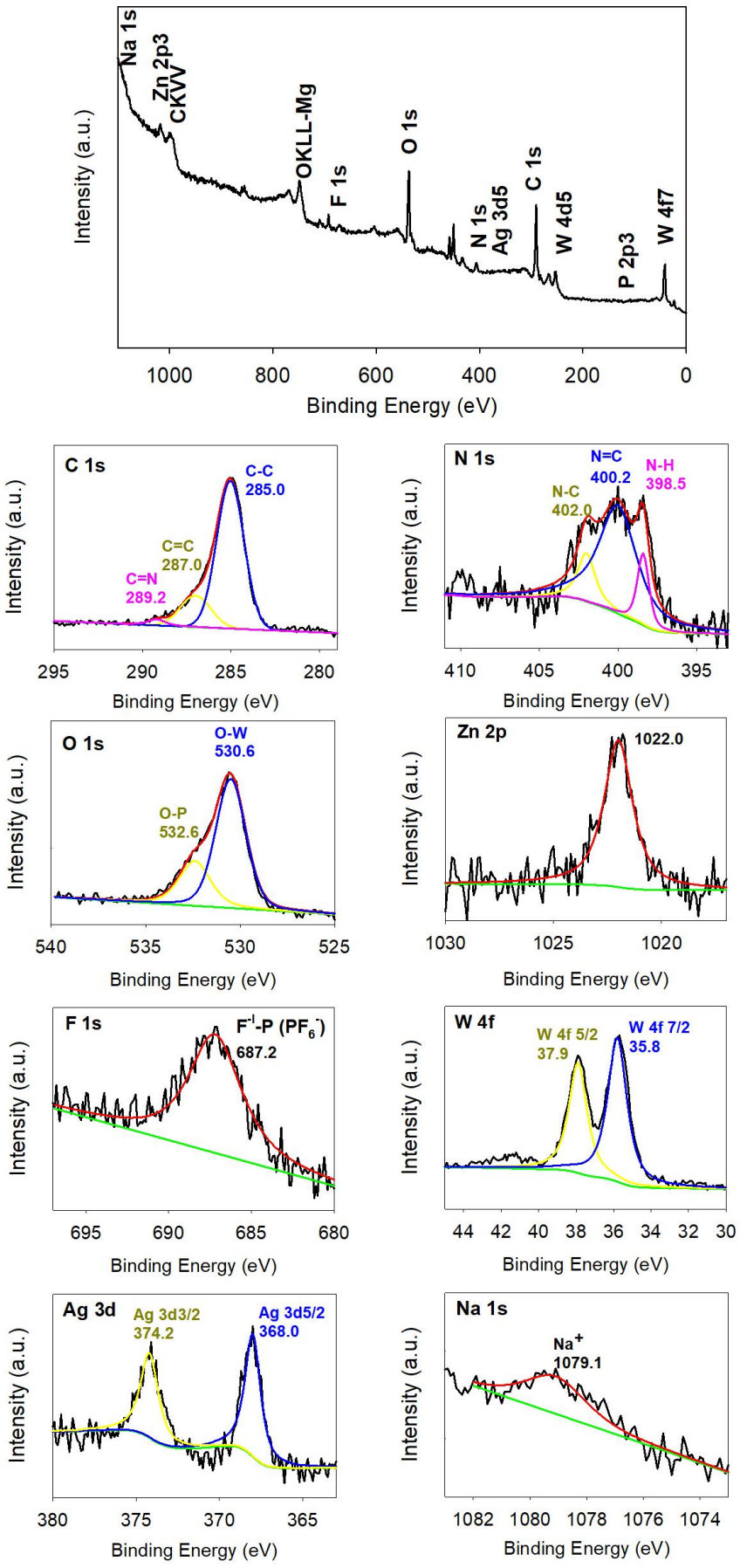

Fig. S19. XPS of **Poly-*cis*-$H_2Py_2Ph_2P$-ZnOEP-P_5W_{30}@Ag** films on ITO.

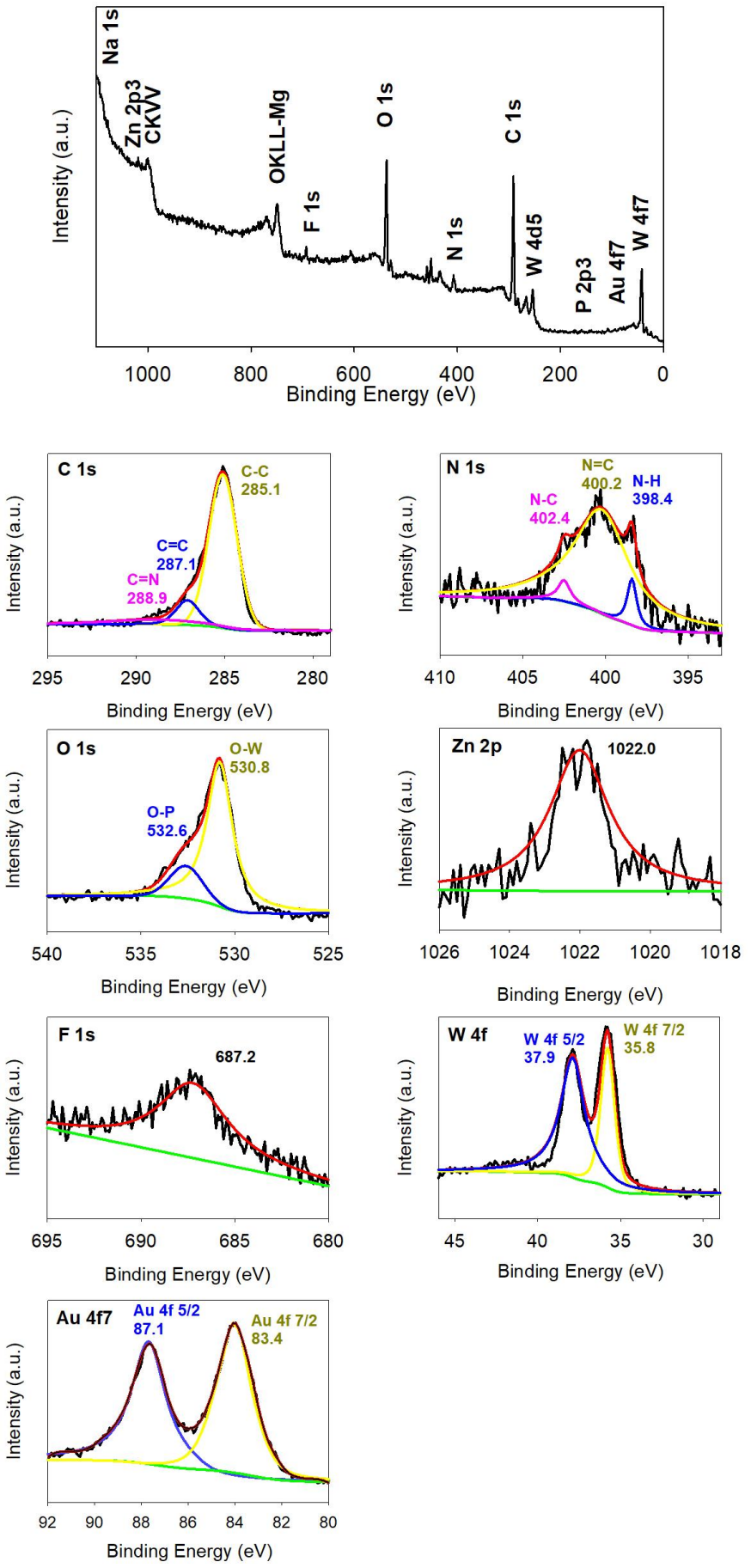

Fig. S20. XPS of **Poly-*cis*-$H_2Py_2Ph_2P$-ZnOEP-P_5W_{30}@Au** films on ITO.

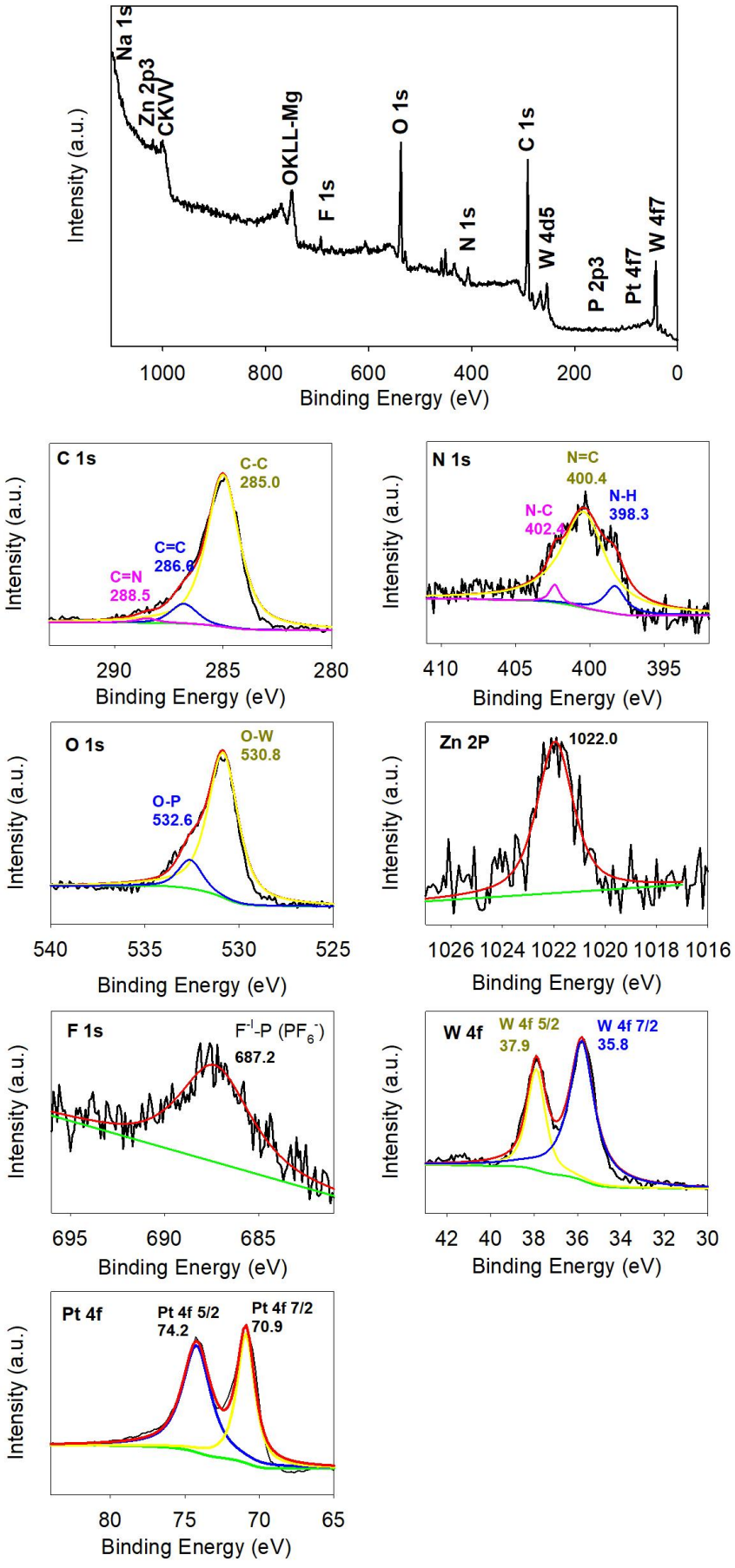

Fig. S21. XPS of **Poly-*cis*-$H_2Py_2Ph_2P$-ZnOEP-P_5W_{30}@Pt** films on ITO.

4.4 SEM images of the Poly-*cis*-$H_2Ph_2Py_2P$-ZnOEP-P_5W_{30}@MNPs films

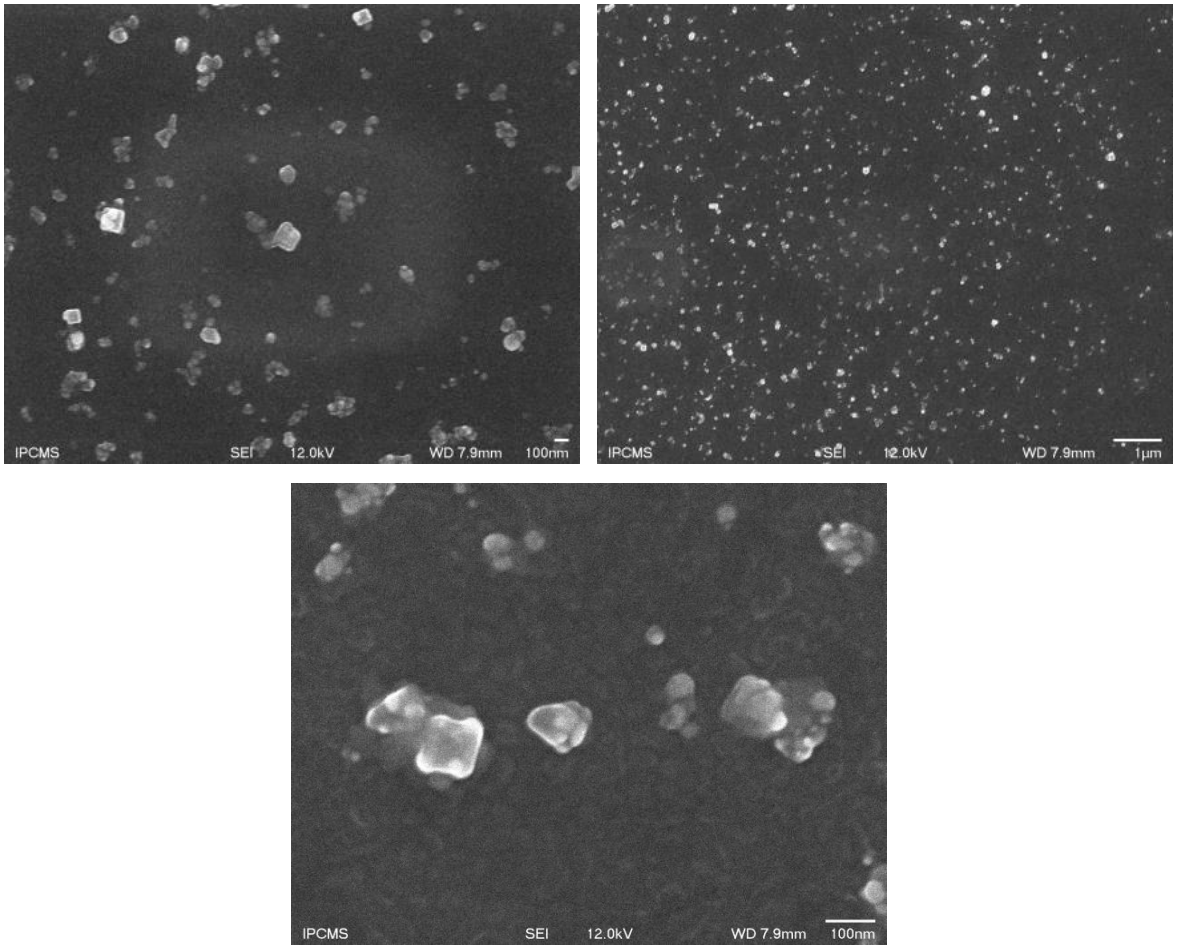

Fig. S22. SEM of **Poly-*cis*-$H_2Py_2Ph_2P$-ZnOEP-P_5W_{30}@AgNPs** on ITO.

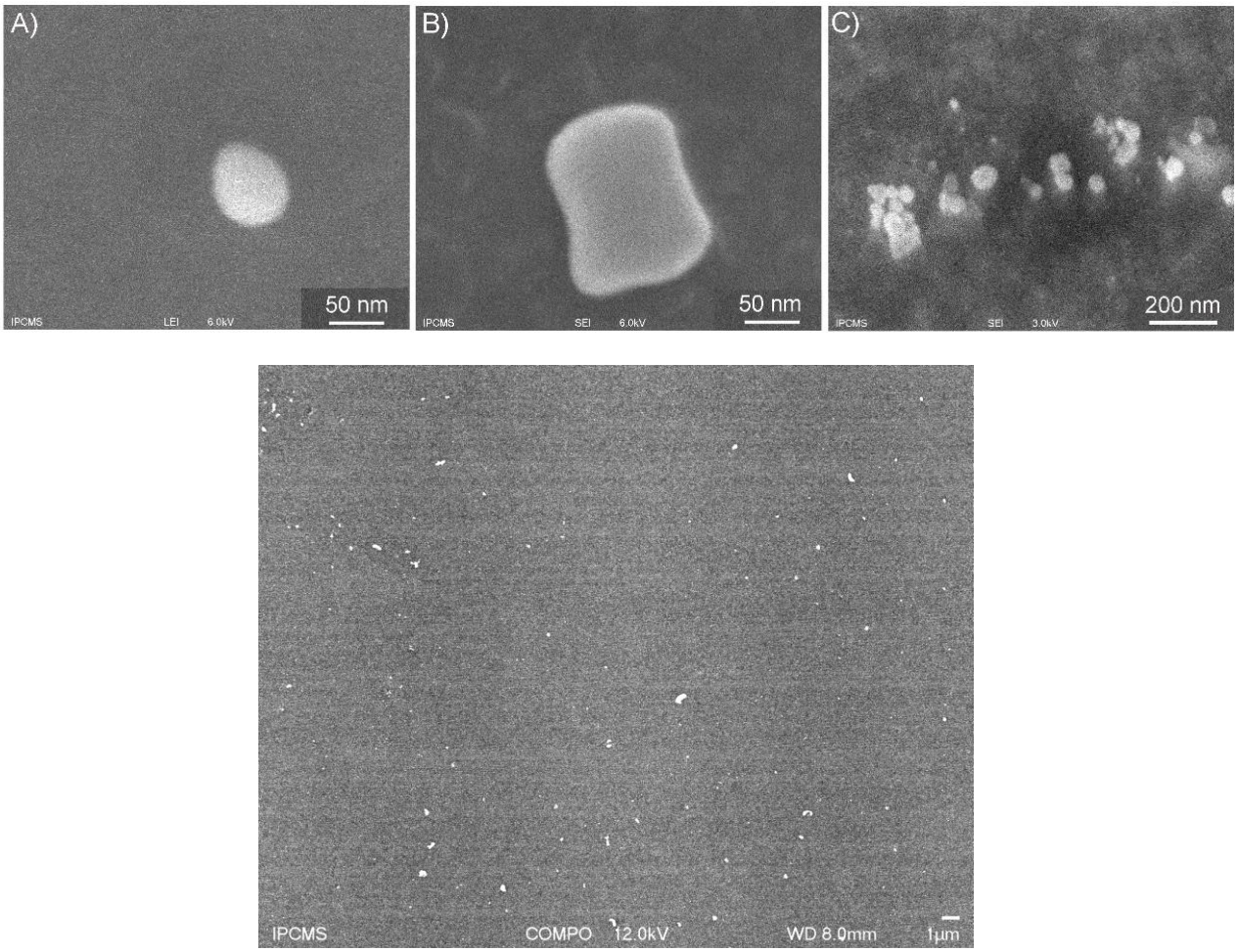

Fig. S23. SEM of **Poly-*cis*-$H_2Py_2Ph_2P$-ZnOEP-P_5W_{30}@Au** on ITO.

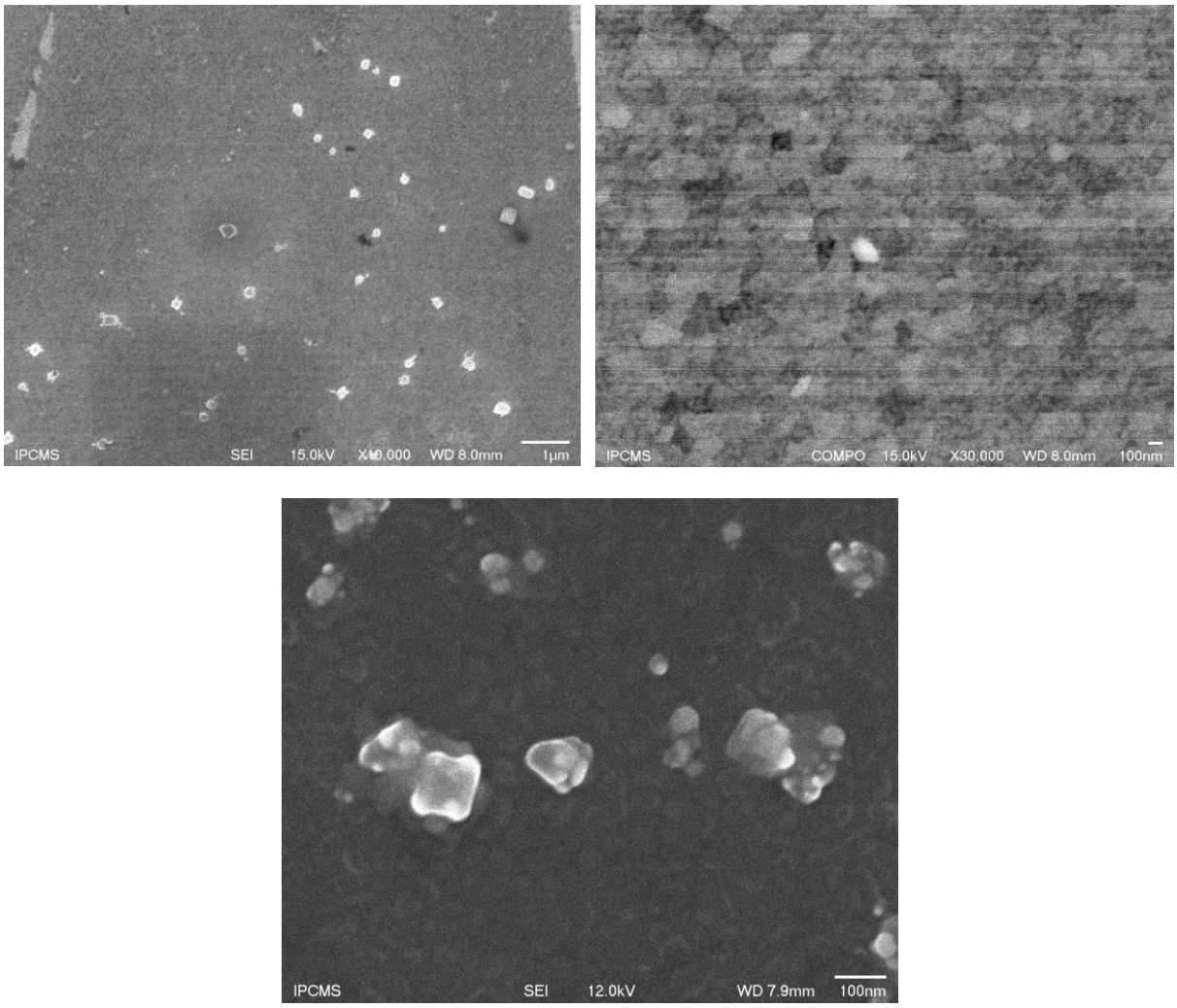

Fig. S24. SEM of **Poly-*cis*-$H_2Py_2Ph_2P$-ZnOEP-P_5W_{30}@Pt** on ITO.

4.5 STEM-EDS elemental color mapping of the Poly-*cis*-$H_2Ph_2Py_2P$-ZnOEP-P_5W_{30}@MNPs films

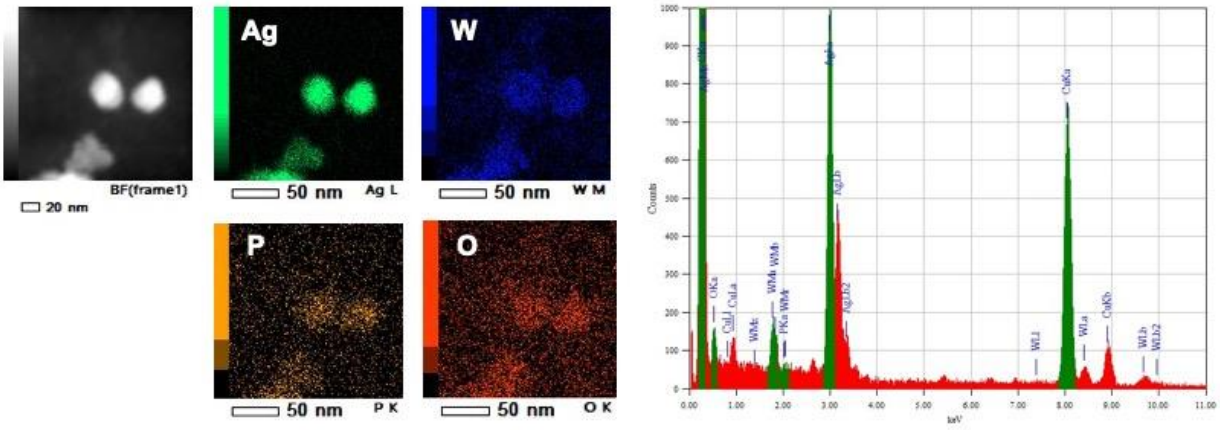

Fig. S25. STEM image, STEM-EDS elemental color mapping of **Poly-*cis*-$H_2Py_2Ph_2P$-ZnOEP-P_5W_{30}@Ag** and Energy-Dispersive X-ray (EDX) analysis. Elemental mapping for silver (green), tungsten (blue), phosphorous (orange) and oxygen (red).

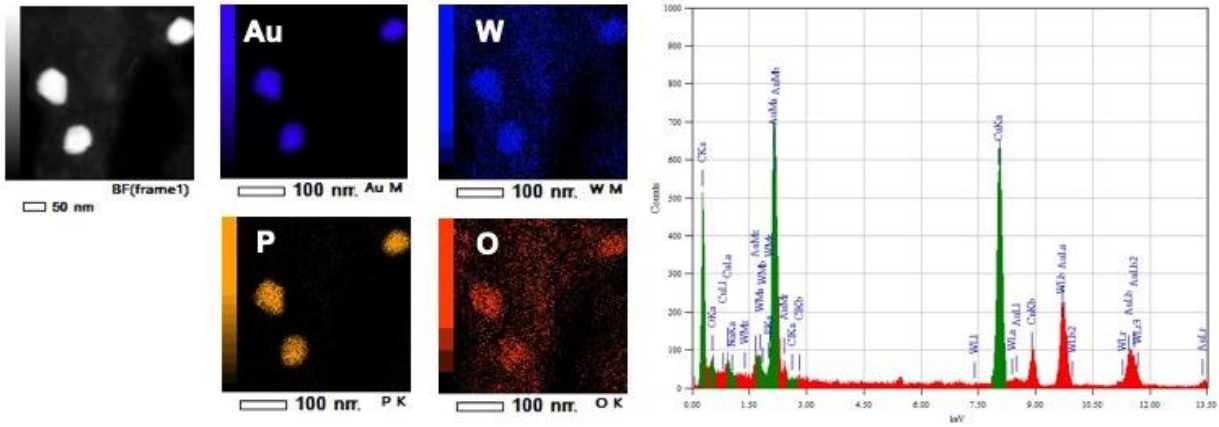

Fig. S26. STEM image, STEM-EDS elemental color mapping of **Poly-*cis*-$H_2Py_2Ph_2P$-ZnOEP-P_5W_{30}@Au** and Energy-Dispersive X-ray (EDX) analysis. Elemental mapping for gold (dark-blue), tungsten (blue), phosphorous orange and oxygen (red).

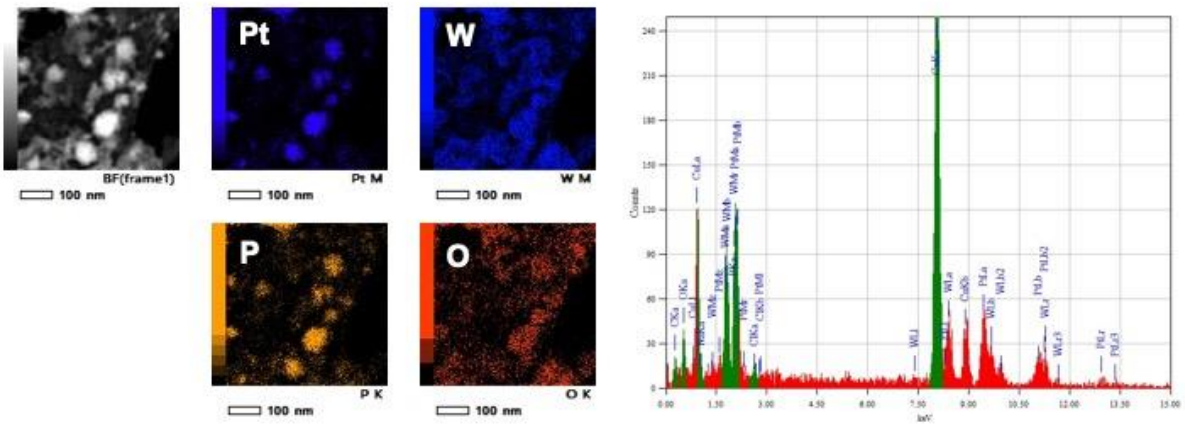

Fig. S27. STEM image, STEM-EDS elemental color mapping of **Poly-*cis*-$H_2Py_2Ph_2P$-ZnOEP-P_5W_{30}@Pt** and Energy-Dispersive X-ray (EDX) analysis. Elemental mapping for platinum (dark blue), tungsten (blue), phosphorous orange and oxygen (red).

4.6 Film Morphology (Atomic Force Microscopy) of Poly-*cis*-$H_2Py_2Ph_2P$-ZnOEP/P_5W_{30}@MNPs films.

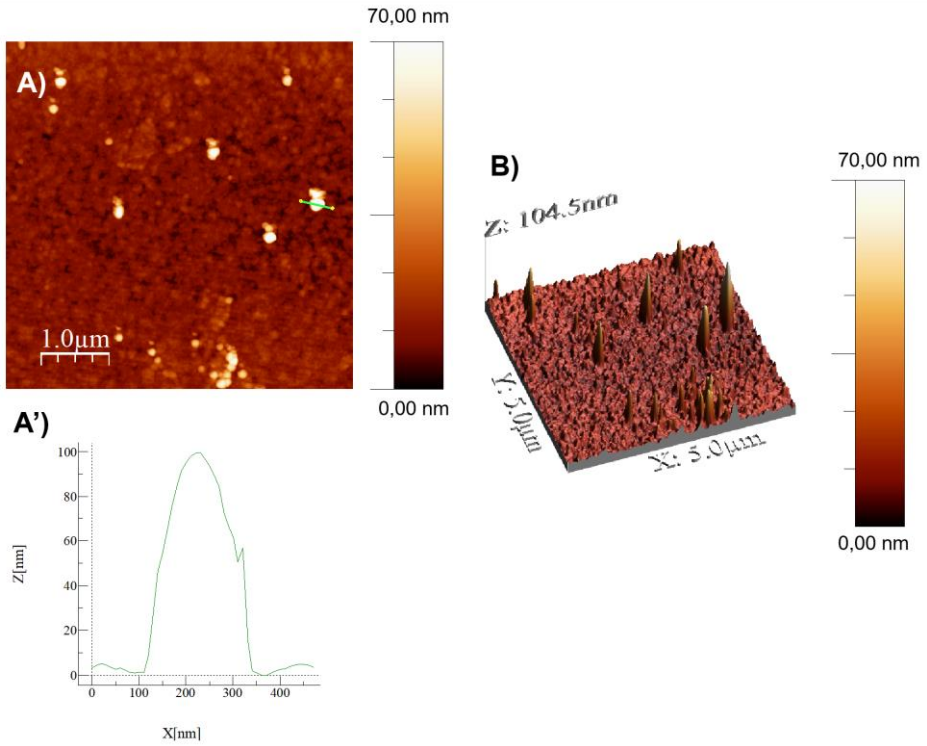

Fig. S28. Tapping mode AFM topography of A) **Poly-*cis*-$H_2Ph_2Py_2P$-ZnOEP/P_5W_{30}@Ag**, and A') section analysis of the aggregate marked by a green line. B) 3D View.

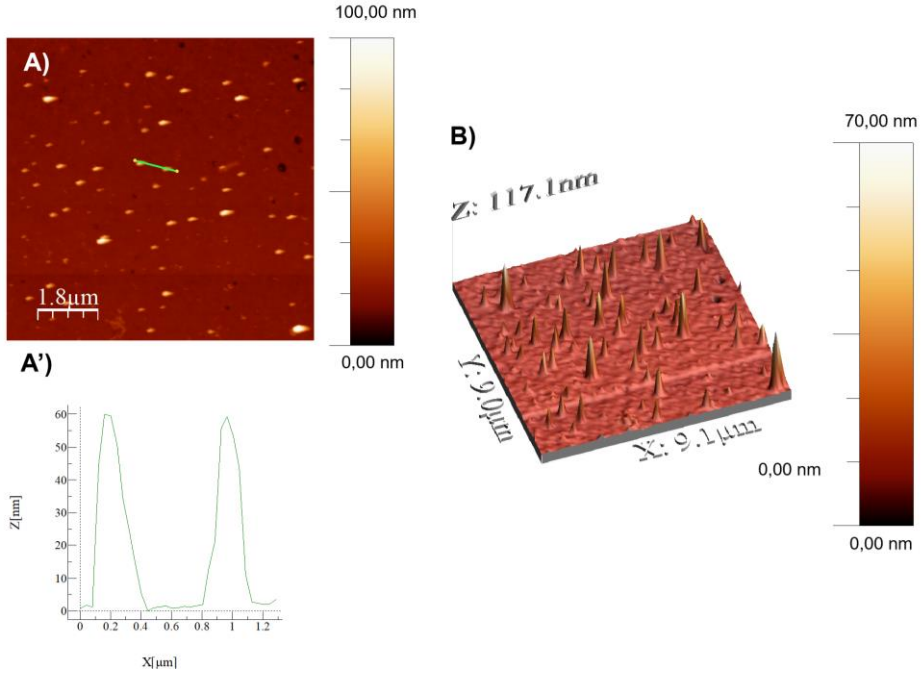

Fig. S29. Tapping mode AFM topography of A) and B) **Poly-*cis*-$H_2Ph_2Py_2P$-ZnOEP/P_5W_{30}@Au**, and A') and B') section analysis of the aggregate marked by a green line. C) 3D View.

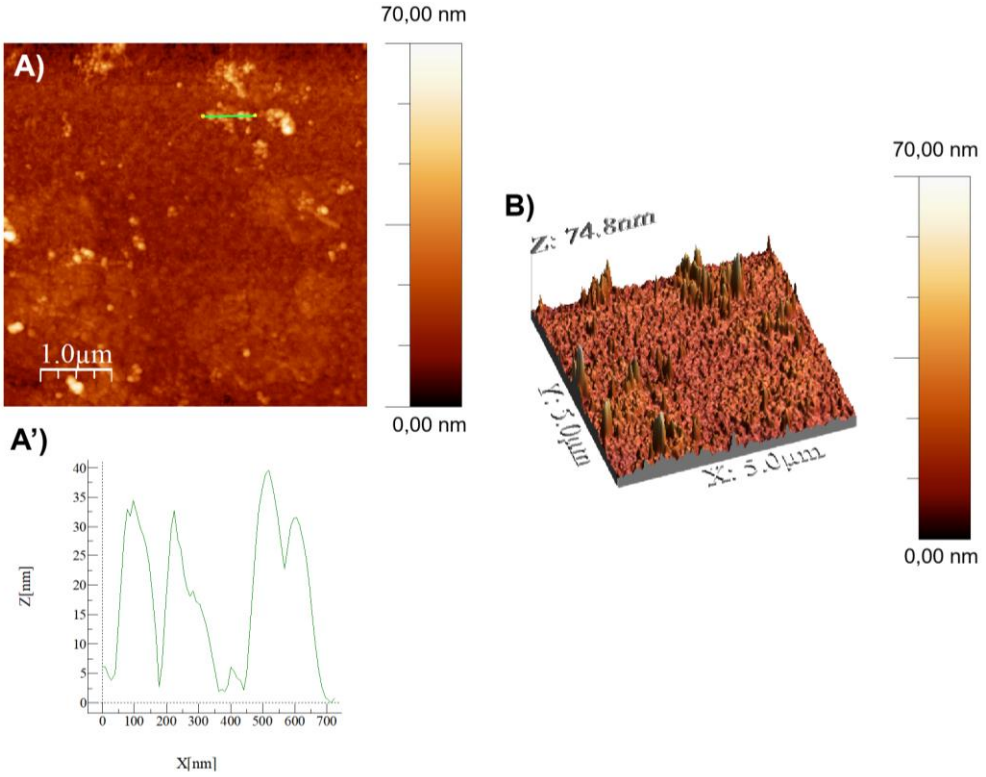

Fig. S30. Tapping mode AFM topography of A) and B) **Poly-*cis*-$H_2Ph_2Py_2P$-ZnOEP/P_5W_{30}@Pt**, and A') and B') section analysis of the aggregate marked by a green line. C) 3D View.

4.7 Electrochemical impedance spectroscopy for Poly-*cis*-$H_2Ph_2Py_2P$-ZnOEP/P_5W_{30}@MNPs

Electrochemical impedance spectroscopy was used to characterize the electronic behaviour of the films. EIS spectra obtained under illumination are shown in Figure S31. In all cases, the influence of mass transport phenomena on the EIS spectra was not observed. In the absence of POM@MNPs the EIS spectra were fitted with the electric circuit in Figure S32. In the presence of POM@MNPs another circuit containing a second R_{ct}, C couple was used to accurately fit the data (Fig. S33). Table S2 contains the values of the parameters of the electric circuits.

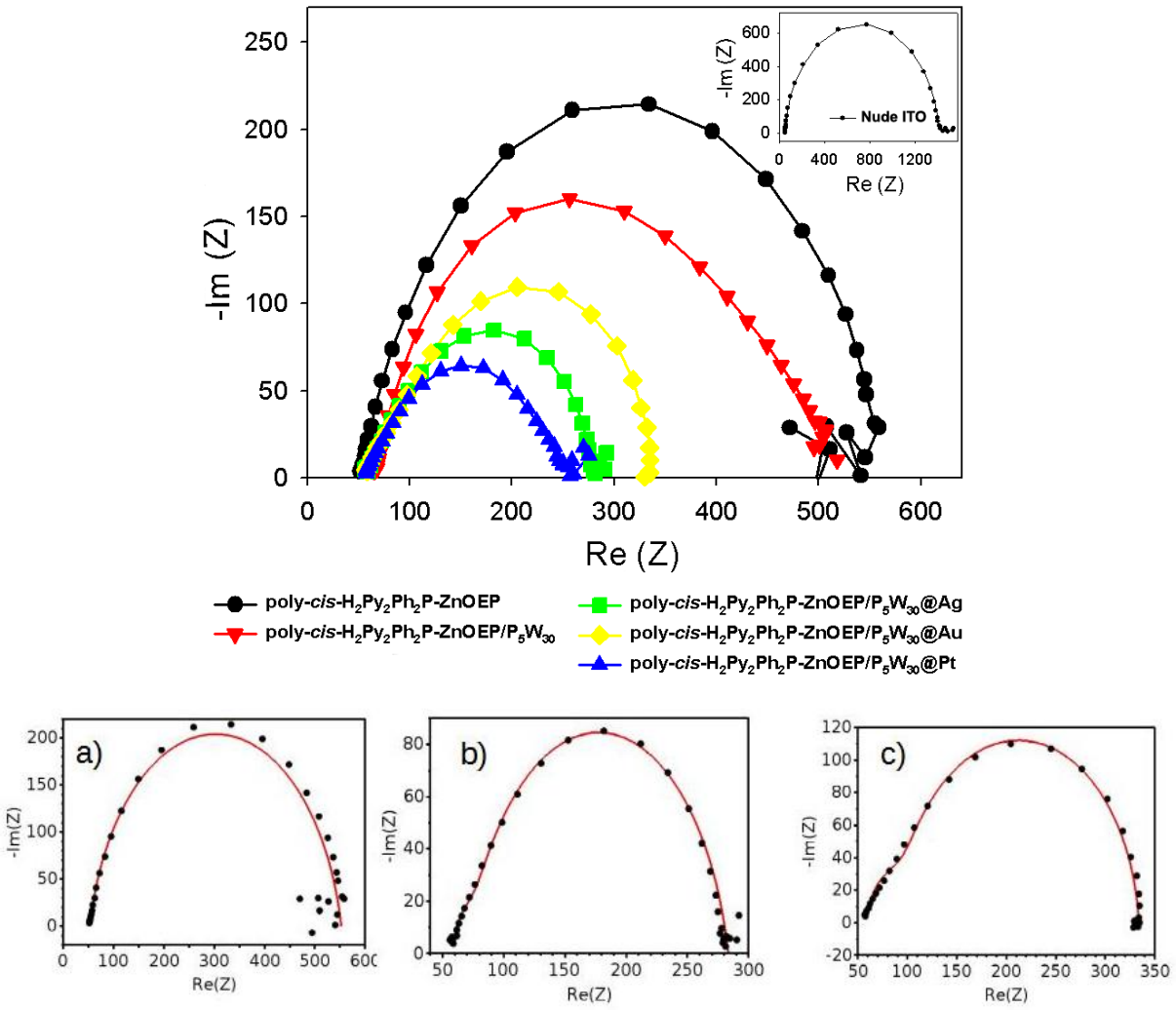

Fig. S31. Electrochemical impedance spectroscopy (EIS) under illumination from a 300 W Xe arc lamp (with λ > 385 nm long pass filter) in H_2O containing I_2 5 mmol L^{-1} and NaI 0.5 mol L^{-1}. The frequency range explored was 0.1 Hz to 10^5 Hz, with the ac amplitude perturbed at 10 mV. DC potential -0.1 V. Fits of the EIS spectra: a) **Poly-*cis*-$H_2Py_2Ph_2P$-ZnOEP**, b) **Poly-*cis*-$H_2Py_2Ph_2P$-ZnOEP/P_5W_{30}@Ag** and c) **Poly-*cis*-$H_2Py_2Ph_2P$-ZnOEP/P_5W_{30}@Au**. Fits of the EIS spectra have been obtained from equivalent circuit represented in Figure S27 for (a) and from equivalent circuit represented in Figure 28 for b) and c). The parameters used for the fit are given in Table S2.

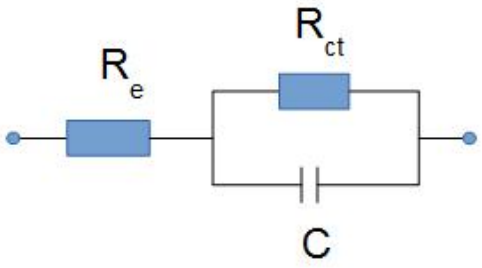

Fig. S32. Equivalent circuit used to model the EIS spectra of **Poly-*cis*-$H_2Py_2Ph_2P$-ZnOEP** films. R_e is the sum of the resistances of the electrolytic solution and of the external circuit, R_{ct} is the charge transfer resistance at the electrode/electrolyte interface and C the capacitance at the electrode/electrolyte interface.

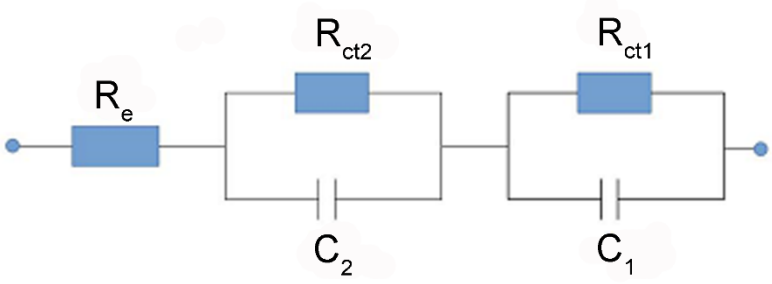

Fig. S33. Equivalent circuit used to model the EIS spectra of **Poly-*cis*-$H_2Py_2Ph_2P$-ZnOEP/P_5W_{30}@MNPs** films. R_e is the sum of the resistances of the electrolytic solution and of the external circuit, R_{ct2} and R_{ct1} can be interpreted as the charge transfer resistances from the solution to the MNPs and from the MNPs to the electrode respectively and C_1 and C_2 the corresponding capacitances.

Table S2. The values of the charge transfer resistances and capacitances determined by the fit of the experimental data.

	Poly-*cis*-$H_2Py_2PH_2P$-ZnOEP	**Poly-*cis*-$H_2Py_2Ph_2P$-ZnOEP/P_5W_{30}**	**Poly-*cis*-$H_2Py_2Ph_2P$-ZnOEP/P_5W_{30}@Ag**	**Poly-*cis*-$H_2Py_2Ph_2P$-ZnOEP/P_5W_{30}@Pt**	**Poly-*cis*-$H_2Py_2Ph_2P$-ZnOEP/P_5W_{30}@Au**
R_e / Ω	53	61	58	57	59
R_{ct1} / Ω	500	444	210	186	239
R_{ct2} / Ω			15	12	35
C_1 /μF	13	28	24	43	14
C_2 /μF			4.5	4.7	3.4
n	0.87	0.76	0.86	0.78	0.94

4.8 Raman spectra of Poly-*cis*-$H_2Py_2Ph_2P$-ZnOEP/P_5W_{30}@MNPs films

For a longer soaking time (9 hours) (Fig. S34) with again **P_5W_{30}@MNPs** solutions, contribution of the **P_5W_{30}** at 966 cm^{-1} became now clearly visible in the spectra. Interaction with Ag NPs did not shift the porphyrin bands. Interaction with Pt NPs shifted a little bit the porphyrin bands towards lower wavenumbers. Films containing gold nanoparticles still exhibited a high sensitivity to light.

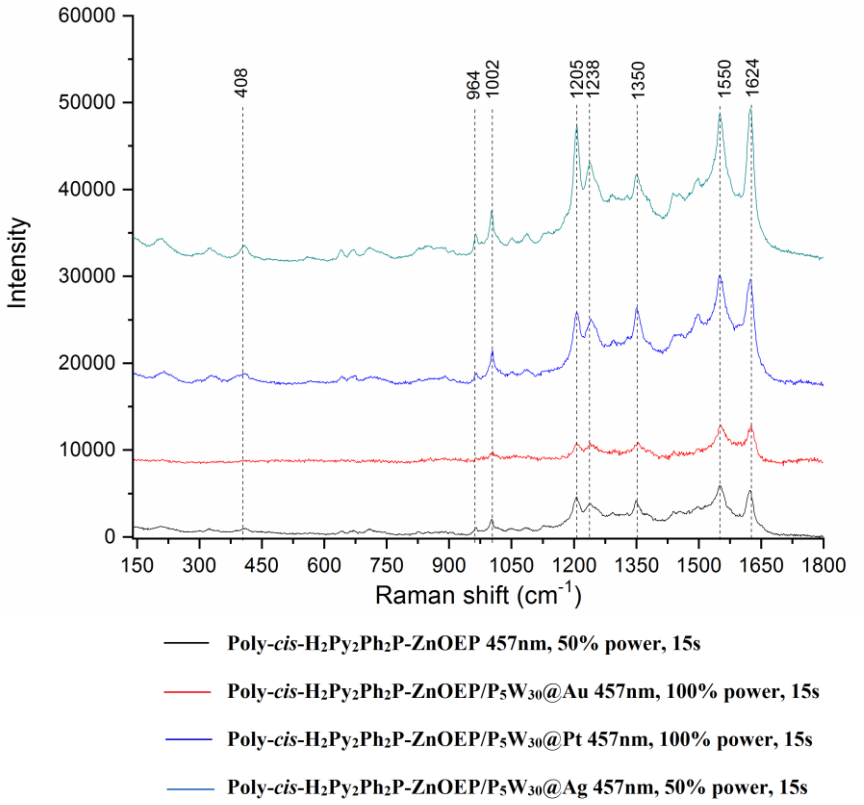

Fig. S34. Raman spectra of **Poly-*cis*-$H_2Py_2Ph_2P$-ZnOEP/P_5W_{30}@MNPs** (0.5 h) excited at 457 nm.

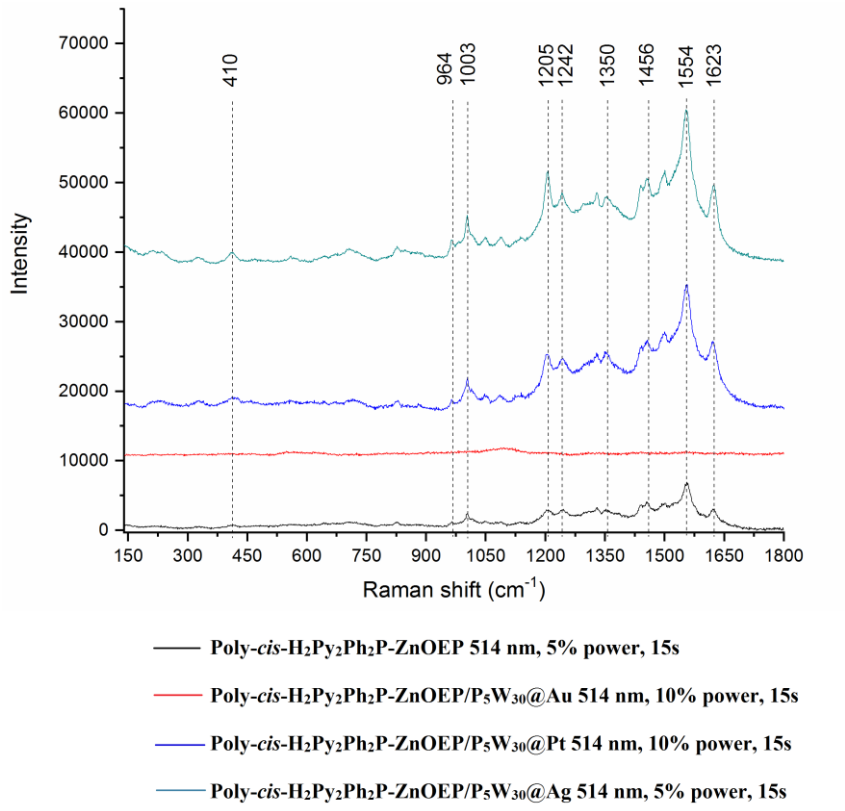

Fig. S35. Raman spectra of **Poly-*cis*-$H_2Py_2Ph_2P$-ZnOEP/P_5W_{30}@MNPs** (0.5 h) excited at 514 nm.

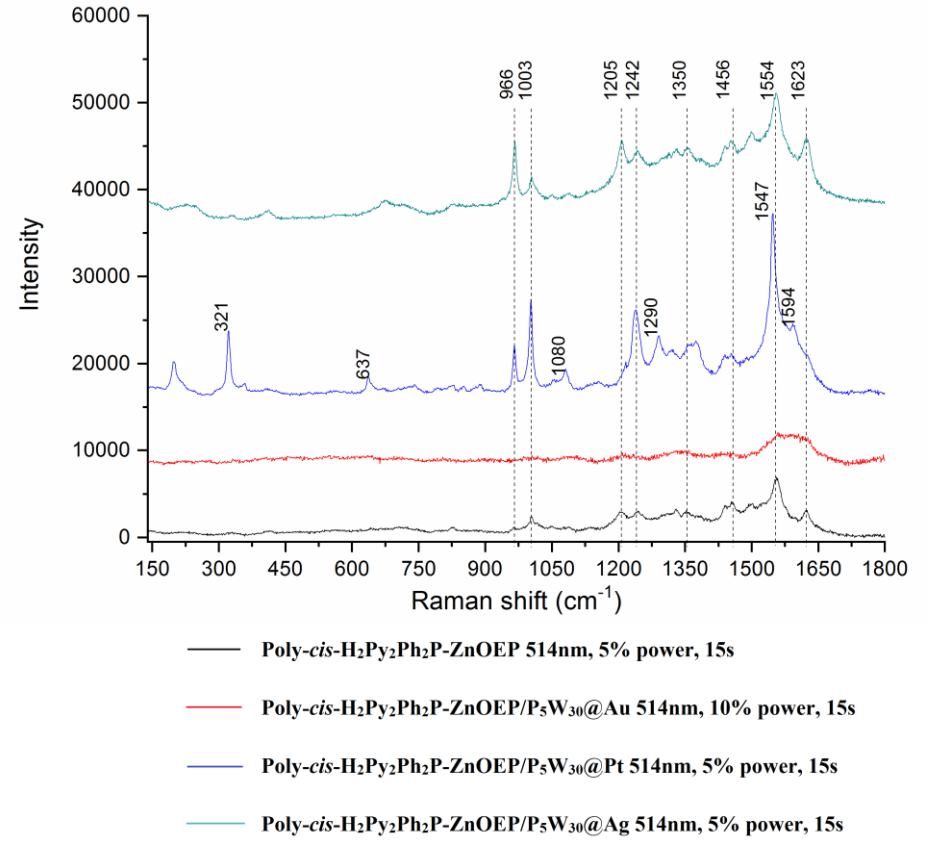

Fig. S36. Raman spectra of **Poly-*cis*-$H_2Py_2Ph_2P$-ZnOEP/P_5W_{30}@MNPs** (9 h) excited at 514 nm.

5. Photocurrent generation by the Poly-*cis*-$H_2Ph_2Py_2P$-ZnOEP/P_5W_{30}@MNPs

5.1 Optimization of the soaking time in P_5W_{30}@AgNPs aqueous solution

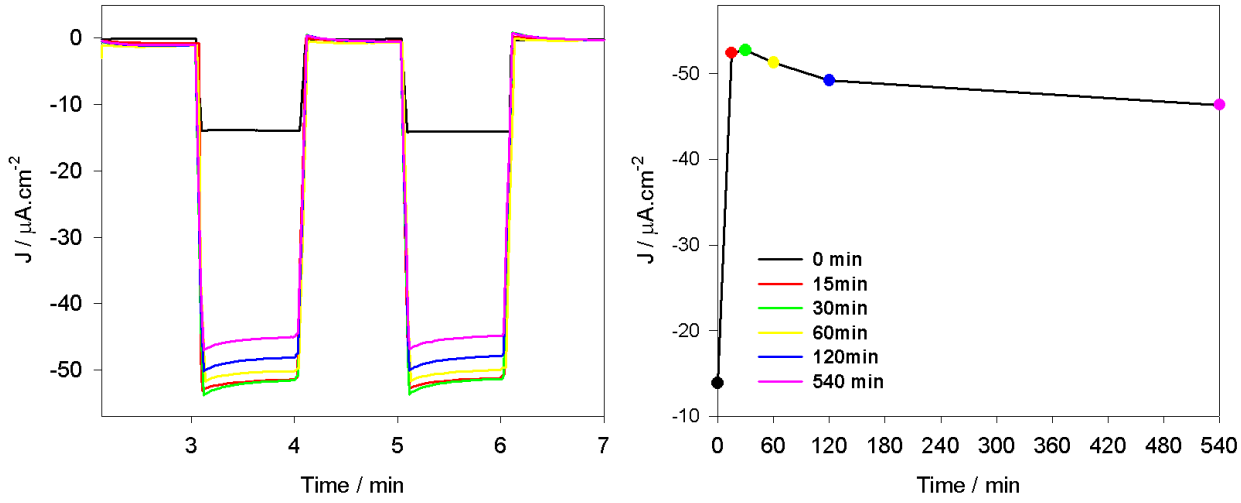

Fig. S37. Photoelectrochemical response of **Poly-*cis*-$H_2Py_2Ph_2P$-ZnOEP** with different soaking time in **P_5W_{30}@AgNPs** solution under on–off light illumination from a 300 W Xe arc lamp (with λ > 385 nm long pass filter) in H_2O containing I_3^- 5 mmol L^{-1} and I^- 0.5 mol L^{-1}. BIAS potential: -0.1 V.

5.2 Effect of noble nanoparticles

Table S3. The magnitude of the photoelectrical responses.

Films	J (µA.cm^{-2})	BIAS	Conditions
Poly-*cis*-$H_2Ph_2Py_2P$-ZnOEP	-13.72	-0.10 V	I_3^-/I^- in H_2O 300 W Xe Arc lamp, λ> 385 nm
Poly-*cis*-$H_2Ph_2Py_2P$-ZnOEP /P_5W_{30}	-18.19		
Poly-*cis*-$H_2Ph_2Py_2P$-ZnOEP /P_5W_{30}@Ag	-54.21		
Poly-*cis*-$H_2Ph_2Py_2P$-ZnOEP /P_5W_{30}@Au	-46.76		
Poly-*cis*-$H_2Ph_2Py_2P$-ZnOEP /P_5W_{30}@Pt	-45.58		

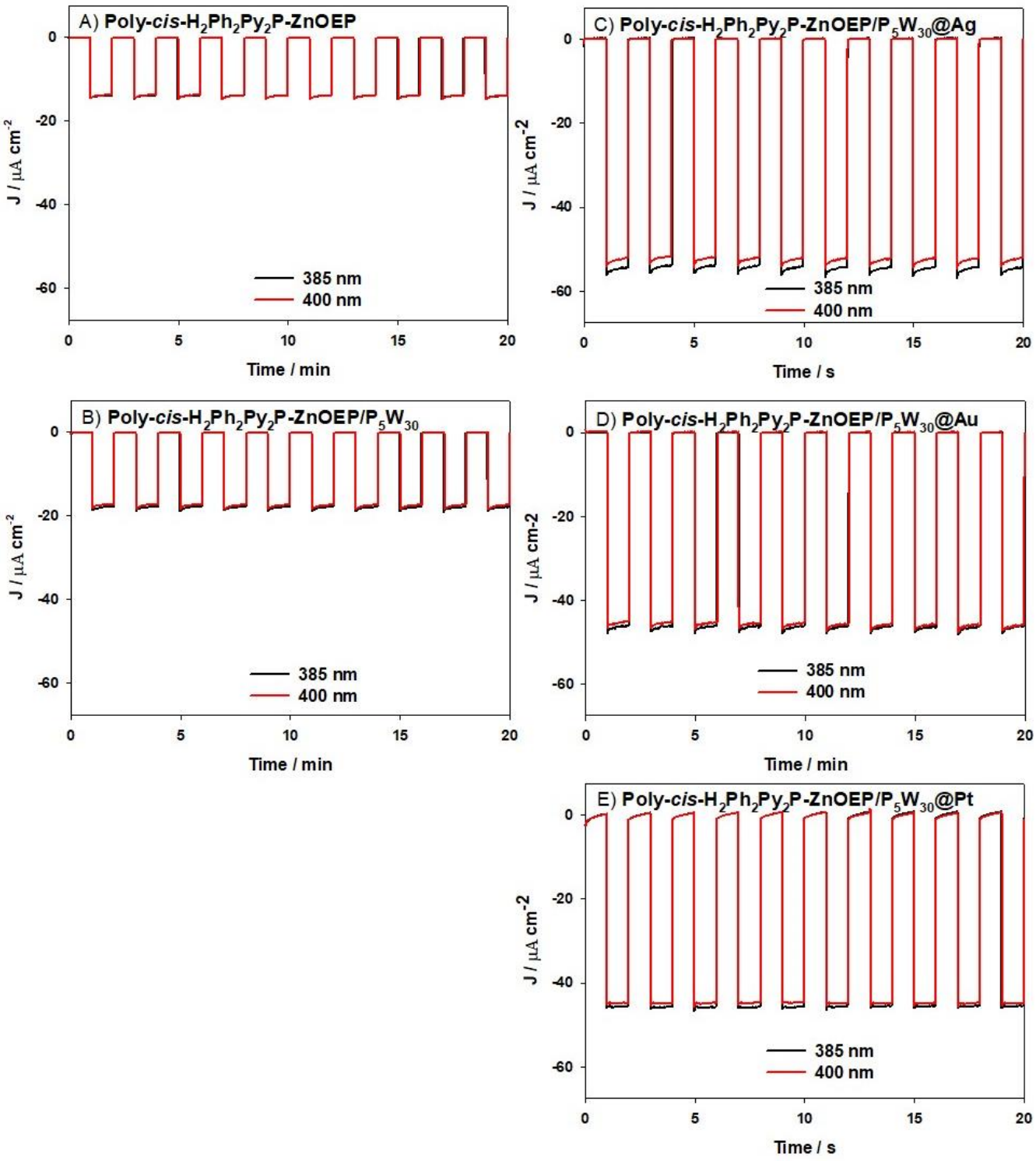

Fig. S38. Comparison of the photoelectrochemical responses under on–off light illumination from a 300 W Xe arc lamp with λ > 385 nm or λ > 400 nm long pass filter) in H_2O containing I_3^- 5 mmol L^{-1} and I^- 0.5 mol L^{-1}. BIAS potential: -0.1 V.

6. Cyclic voltammogram of the films and of P_5W_{30}

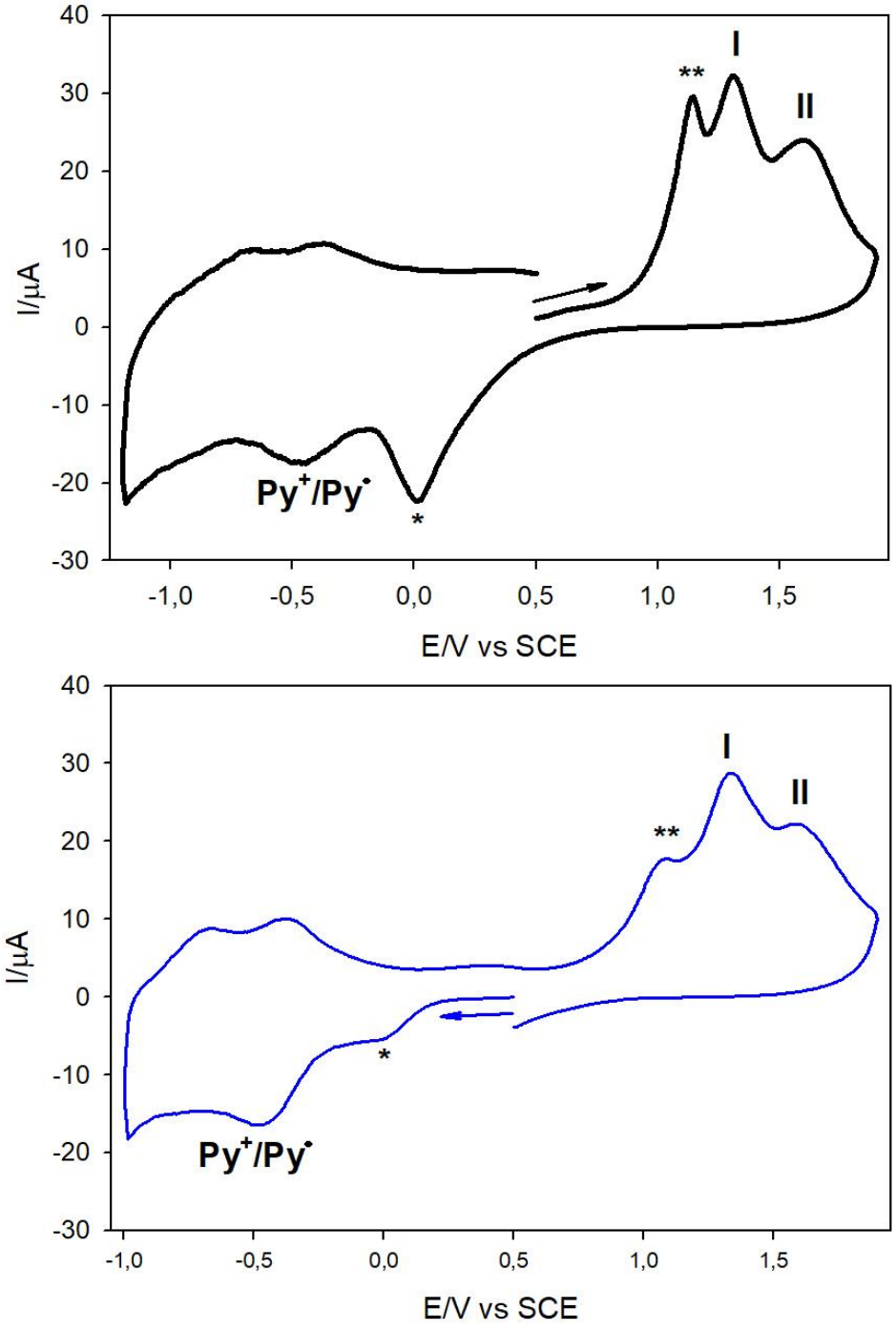

Fig. S39. CVs of **Poly-*cis*-$H_2Py_2Ph_2P$-ZnOEP** modified ITO electrodes in CH_3CN containing 0.1 M of $TBAPF_6$ and 0.5 mol L^{-1} NaI. WE surface = 1 cm^2; scan rate: 10 mV s^{-1}.

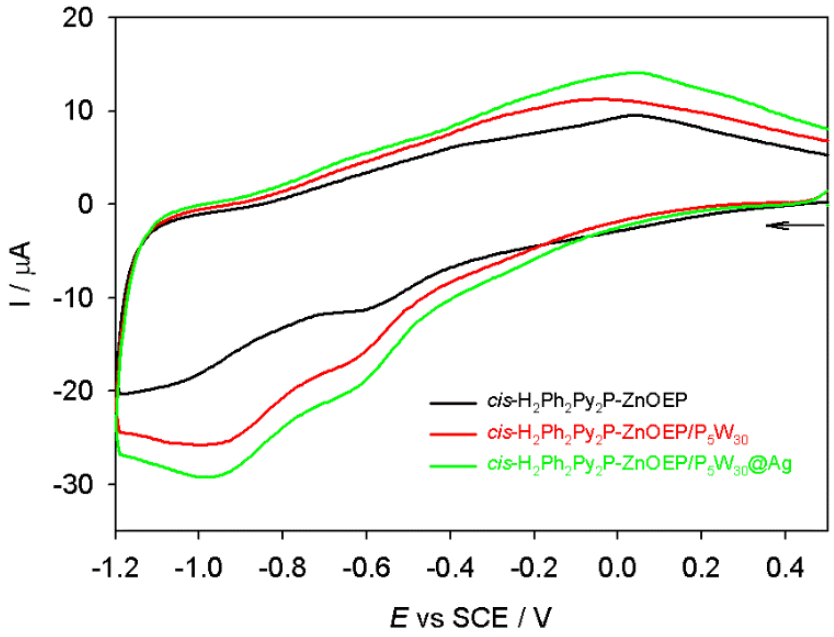

Fig. S40. CVs of **Poly-*cis*-$H_2Py_2Ph_2P$-ZnOEP** (black curve), **Poly-*cis*-$H_2Py_2Ph_2P$-ZnOEP/P_5W_{30}** (red curve), and **Poly-*cis*-$H_2Py_2Ph_2P$-ZnOEP/P_5W_{30}@Ag** (green curve) (with 30 min soacking time in P_5W_{30}@AgNPs aquesous solution) modified ITO electrodes in H_2O containing 0.5 mol L^{-1} NaI. WE surface = 1 cm^2; scan rate: 20 mV s^{-1}.

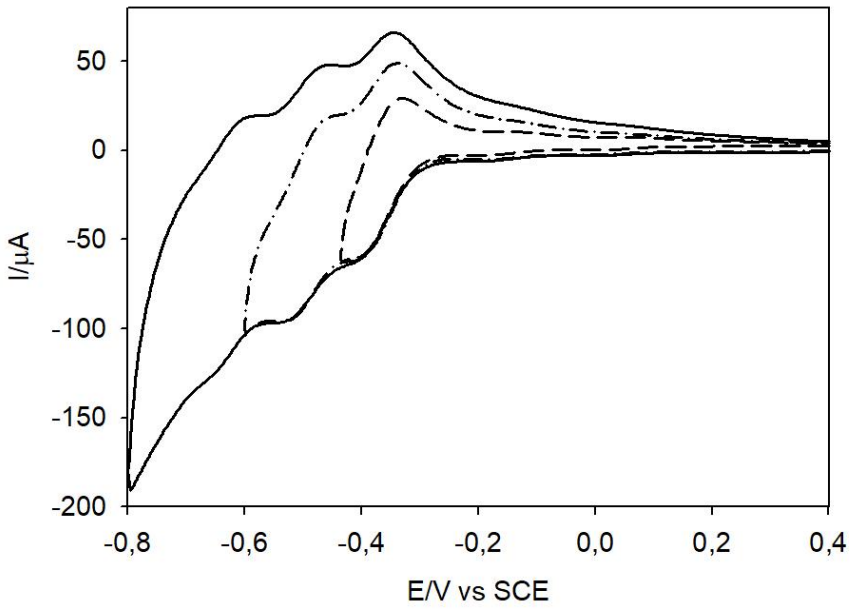

Fig. S41. CVs of **$K_{14}[NaP_5W_{30}O_{110}]$** in H_2O containing 0.5 mol L^{-1} NaI. Working electrode: GC, surface = 0.07 cm^2; scan rate: 0.02 V s^{-1}.